Version of Record: https://www.sciencedirect.com/science/article/pii/S0272771421003668
Manuscript_e0fef718ade7e704a1319e41237bb6df

Improved Modeling of the Role of Mangroves in Storm Surge Attenuation

Qiang Chen[a], Yuepeng Li[a,*], David M. Kelly[b], Keqi Zhang[a], Brian Zachry[c], Jamie Rhome[c]

[a] *Coastal Research Lab., International Hurricane Research Center, Florida International University, Miami, Florida, 33199, USA*
[b] *Centre for Environment, Fisheries and Aquaculture Science (CEFAS), Lowestoft, NR33 0HT, UK*
[c] *National Hurricane Center, National Weather Service, National Oceanic and Atmospheric Administration, Miami, Florida, 33165, USA*

Abstract

Mangroves have been proven to be effective in storm surge attenuation but it remains an important challenge to accurately quantify such bio-shielding effects using numerical simulations, as it is very difficult to comprehensively represent the ecological characteristics of mangroves at both large and small scales. In this study, a numerical method is developed and implemented in the Coastal and Estuarine Storm Tide (CEST) model in order to investigate the attenuation effect of mangroves on storm surge. This numerical method employs an improved drag force formula, which involves the development of new abstract tree models and use of a landscape scale data map of mean mangrove tree height for the study area. The storm surge observed in the South Florida mangrove zone caused by Hurricane Wilma (2005) is used to verify the numerical model. The numerical results indicate a maximum surge of approximately 4.3 m, and a decay rate of peak storm surge height of approximately 18 cm/km across the areas with a mixture of mangrove islands and open water, and nearly 24 cm/km through areas with dense mangrove forest. Results also show that short mangroves (< 4 m) can outperform tall mangroves on surge attenuation when the water depth is low (< 4 m). Extensive comparisons are also made with the conventional Manning coefficient based method that incorporates the mangrove drag force into bed friction; it is found that the current method predicts better inundation extents for Wilma (2005), hence a more accurate quantification of the attenuation of storm surge due to mangroves.

Keywords: Storm Surge, Mangrove, Nature-Based Infrastructure, Hurricane Wilma (2005), Manning Coefficient, Drag Force

*Corresponding author.
Email addresses: qchen@fiu.edu (Qiang Chen), yuepli@fiu.edu (Yuepeng Li)

1. Introduction

Mangrove forests, as a sustainable and ecological alternative to conventional coastal engineering defences, protect human lives and infrastructures from not only the damaging winds induced by hurricanes but also currents and waves such as storm surge and tsunami (Tanaka et al., 2007; Zhang et al., 2012; Tanaka, 2009; Teh et al., 2009; Xu et al., 2010; Zhang et al., 2013; Temmerman et al., 2013; Rodríguez et al., 2017; Sheng and Zou, 2017; Iimura and Tanaka, 2012). Mangroves can significantly dissipate wind-generated short-period waves in a few hundred meters into the forest (Horstman et al., 2014; Zhang et al., 2020), but need much longer distance (in kilometers) to reduce long-period waves such as storm surge (Xu et al., 2010; Zhang et al., 2012). Currently, accurate quantification of mangrove effects on storm surge propagation still remains a challenging topic of practical interests. Research efforts on this include field survey (Smith et al., 2009; Krauss et al., 2009), physical modeling (Iimura and Tanaka, 2012; Tomiczek et al., 2020), and numerical modeling (Xu et al., 2010; Zhang et al., 2012). While field survey and physical modeling are very expensive, time-consuming and site-limited, numerical modeling as a cost-effective and reliable solution has become more and more popular (Wu et al., 2001; Zhang et al., 2012; Liu et al., 2013; Iimura and Tanaka, 2012; Wu and Marsooli, 2012; Rodríguez et al., 2017; Sheng and Zou, 2017; Teh et al., 2009; Xu et al., 2010; Zhang et al., 2013). Numerical models that resolve atmosphere-ocean-coast interactions would provide a powerful, low-cost, and flexible tool for the designing and management of mangrove zones against real-world storm surges.

For numerical modeling, typical approaches for handling mangrove-fluid interactions fall into two categories: 1) estimate the drag force by mangroves to the flows via the Manning coefficient based bed friction force (Liu et al., 2013; Rodríguez et al., 2017; Xu et al., 2010; Zhang et al., 2012, 2013), and 2) treat mangroves as vertical cylinders (or similar assumptions) informed by mangrove characteristics, and consider the volume exclusion term (owing to partial occupation of the flow space by mangroves) and mangrove hydrodynamic impact based on the Morison's equation (or its variants) (Mazda et al., 1997; Wu et al., 2001; Teh et al., 2009; Wu and Marsooli, 2012; Iimura and Tanaka, 2012). Despite being physically unjustified, the Manning coefficient based method is feasible and easy to implement, and has achieved reasonable performance since both the drag force and the bed friction force share the same quadratic relationship with flow velocity. In particular, Zhang et al. (2012) suggested using an enhanced Manning coefficient map to account for the effects of different land covers on storm surges, where a Manning coefficient of 0.14 was used for the mangrove forest. Nevertheless, the Manning coefficient based method ignores the mangrove physical

characteristics such as stem size, tree height, and tree density. In contrast, the approaches in the second category are able to take into consideration the mangrove characteristics but often requires development of sophisticated tree architecture models (for computing local mangrove hydrodynamic forces) and incorporation of the data of mangrove characteristics at large scales (for computing regional mangrove hydrodynamic impact). However, designing an informative and computationally suitable abstract tree model is not straightforward, due to the complexity nature of mangrove tree structure. The abstraction of mangrove trees to uniform cylinders represents a significant simplification in estimating the effect of mangrove tree shape on water flows, especially for red mangroves which are famous for their tangled roots called "prop-roots". Nevertheless, for the black mangroves, identified by their pencil roots, the abstract tree model used by Teh et al. (2009) that includes root, stem and leaf, formed by vertical cylinders of different diameters and heights determined by field measurements, appears to represent the tree structure well.

In addition to designing appropriate tree architecture models, another difficulty of the above-mentioned second category approach is the employment of large scale data maps of mangrove characteristics, such as spatial variations of tree height, stem size and density. Previous numerical studies in this category are usually based on estimations or field measurements in small plots for the mangrove characteristics, and few researches have exploited the landscape scale data until recently. For example, Zhang et al. (2020) investigated the short-period wave attenuation by mangroves at the Daguansha of Beihai city, China, through solving a power-dissipation based wave attenuation equation that makes use of the remote sensing and field measurement data of landscape mangrove characteristics, such as mangrove species, crown breadth and tree height. In fact, with the advancement of remote sensing technology, surveys of mangrove forests, particularly tree heights and extents, at the landscape scale have become feasible (Simard et al., 2006; Feliciano et al., 2017; Zhang et al., 2016; Ruiz et al., 2017, 2018). As an example, Simard et al. (2006) used the Shuttle Radar Topography Mission elevation data to produce a map of mean tree height for the mangrove forest at the Gulf Coast of South Florida, USA. With this tree height data map, it is possible to obtain the data maps of mangrove stem size and density that are required by the aforementioned mangrove-fluid interaction approaches, as many ecological studies on mangroves have indicated that there are strong allometric relationships between stem size and tree height (Tamai et al., 1986; Hirata et al., 2014; Mugasha et al., 2019), between stem size and stem density (Ward et al., 2006), and between stem size and biomass (Ross et al., 2001; Smith and Whelan, 2006).

The objective of this paper is thus to investigate the effect of mangroves on storm surge attenuation via an improved numerical modeling approach, which incorporates a new tree architecture model for red mangroves, that is designed based on the field measurements of the individual components of biomass (e.g., roots, stems, branches and leaves), and landscape scale mangrove characteristics developed based on remote sensing data of mangrove tree height and mangrove allometric equations. The numerical simulations are based on the Coastal and Estuarine Storm Tide (CEST) model (Zhang et al., 2012), which is well verified for tide and storm surge simulation through historical hurricane events, such as Wilma (2005) (Zhang et al., 2012; Liu et al., 2013), Andrew (1992) (Zhang et al., 2013), and Hugo (1989) and Camille (1969) (Zhang et al., 2008). In these papers, however, CEST employed the Manning coefficient based method to account for mangrove effects. Therefore, this study also aims to provide an in-depth comparison between the newly developed mangrove characteristics based method and the existing Manning coefficient based method.

The paper is organized as follows: Section 2 presents the study area, the landscape scale data map of mangrove mean tree height, and the allometric equations for mangrove characteristics; Section 3 gives an overview of the CEST model as well as the detailed implementation of the mangrove tree component; Section 4 examines the numerical model using an idealized test case and compares the fundamentals of the current method for mangrove modeling with the Manning coefficient method; Section 5 describes the simulation of Hurricane Wilma (2005) using both the current method and the Manning coefficient method for mangroves; Section 6 is for discussions; Section 7 draws conclusions.

2. Study area and data

2.1. Study area

The mangrove forest distributed along the Gulf coast of South Florida, USA, provides an ideal site for investigating mangrove attenuation effect on storm surge (see Fig. 1). South Florida suffers from frequent tropical storm impact during hurricane season, and the gently-sloped topography makes it vulnerable to inundation induced by storm surges. The mangrove zone as indicated in Fig. 1 covers a coastline of 200 km stretching from Naples to the north coast of Florida Bay. The mangrove species dominating this area are the red mangrove (*Rhizophora mangle*), black mangrove (*Avicennia germinans*), and white mangrove (*Laguncularia racemosa*) (Ruiz et al., 2017, 2018), with tall trees (> 4 m) living along the coast area while short scrubs distributed further inland (Fig. 3). Recent hurricanes that have struck this mangrove zone include Andrew (1992), Wilma (2005) and Irma (2017)

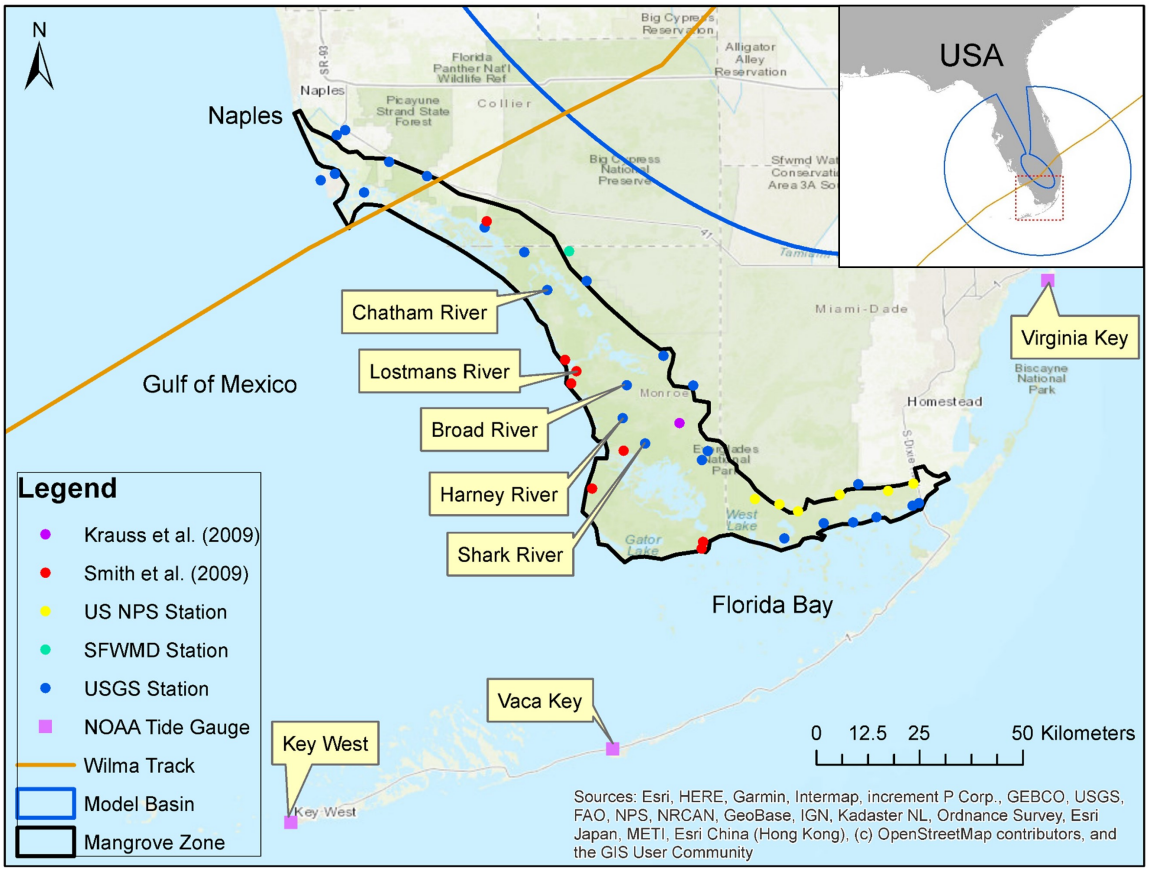

Fig. 1: The study area, with the basin for the numerical model and the measurement locations for Hurricane Wilma (2005).

(Fig. 2). Particularly, this study focuses on the numerical simulation of Hurricane Wilma (2005). Wilma approached the South Florida from the southwest and made landfall as a Category 3 hurricane around 10:30 coordinated universal time (UTC) on 24 October 2005 near Cape Romano. Wilma was moving at a forward speed of approximately 37 km/h when the landfall of the center occurred, with the maximum sustained winds estimated to be near 194 km/h (Pasch et al., 2006). Despite being weaker at landfall (Category 3), Wilma had an extraordinarily wide eye of 89-105 km in diameter and a track at the upper part of the mangrove zone, leading to significant storm surge (approximately 5 m at maximum (Smith et al., 2009)) and extensive coastal inundation. According to the field survey by Smith et al. (2009), Wilma completely destroyed the Lostmans Ranger Station (located at the north shore of the Lostmans River mouth) that survived the passage of the Labor Day

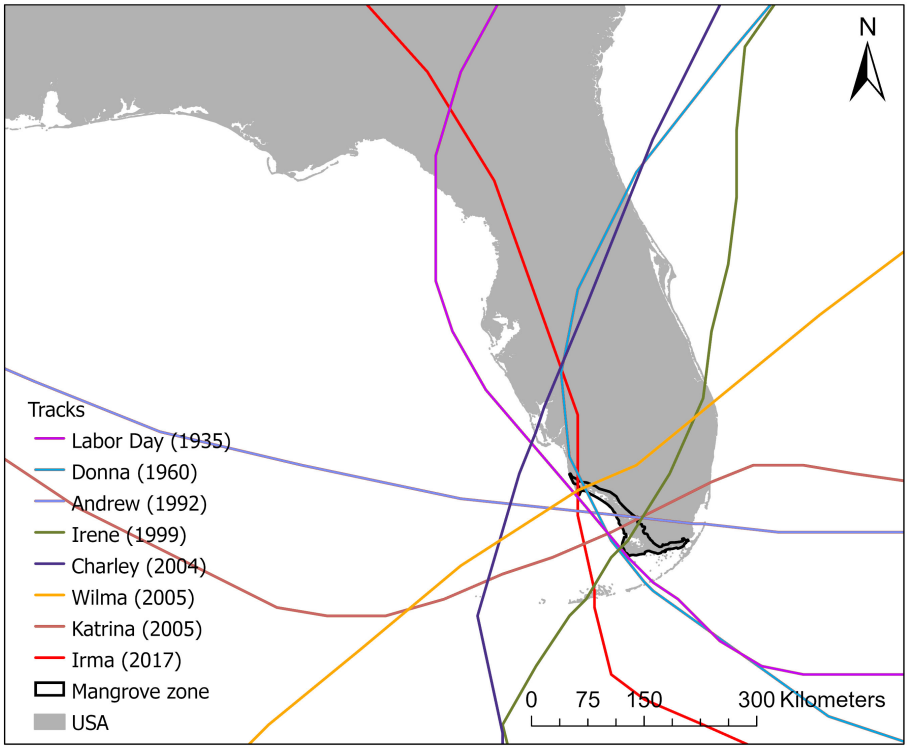

Fig. 2: Tracks of relevant hurricanes that have impacted the mangrove zone at the Southwest Florida USA.

Storm (1935), Hurricane Donna (1960), and the leading and trailing eyewalls of Hurricane Andrew (1992) (Fig. 2).

Extensive storm surge measurements during and after Wilma (2005) were made by a variety of institutions and many individual researchers. In particular, the data collected for verifying the current numerical simulations include: (1) high water marks (HWMs) and time series of water levels collected at the U.S. Geological Survey (USGS) stations (Soderqvist and Byrne, 2007; Telis, 2006), U.S. National Park Service (NPS) stations (Telis, 2006), South Florida Water Management District (SFWMD) stations (Telis, 2006) and from field survey by individual researchers (Smith et al., 2009; Krauss et al., 2009); (2) time series of water elevations measured at National Oceanic and Atmospheric Administration (NOAA) tide gauges. Fig. 1 shows the locations of these measurements. For other data sources of Hurricane Wilma (2005) (e.g. HWMs collected by Federal Emergency Management Agency (FEMA) along the Florida Keys), the reader is referred to the previous work of Zhang et al. (2012).

2.2. Landscape scale mangrove data map

The structural data of mangroves such as tree height, stem size and density plays an important role in quantifying the effect of mangroves on storm surge attenuation. For the current numerical simulations, a landscape scale data map of mean mangrove tree height for the study area (see Fig. 1) was obtained with the following procedure using airborne Light Detection And Ranging (LiDAR) data collected by the Florida Department of Emergency management in 2007 (Fig. 3). First, the LiDAR data in binary LAS format was downloaded from the coastal data website of NOAA (https://coast.noaa.gov/dataviewer/#/lidar/search/, accessed 28 December 2019). Second, the Digital Surface Model (DSM) and Digital Terrain Model (DTM) with a pixel spacing of 15 m reference to State Plan HARN NAD83 horizontal datum and NAVD88 vertical datum in units of meters were generated for the mangrove zone by interpolating the LiDAR points. The first return and ground LiDAR measurements were used to produce DSM and DTM, respectively, by using the inverse distance weighted interpolation in ArcGIS (www.esri.com). Third, the Digital Canopy Model (DCM) was generated by subtracting the DTM from DSM. The values of DCM could be negative in the areas without many trees because of the difference in LiDAR points used for DSM and DTM interpolations and the negative values in DCM were set to be zero. The mangrove zone (Fig. 3) for the calculation of DCM was the same as that used by Zhang et al. (2012). Finally, the mean tree height for each model grid cell were computed using the DCM pixels falling within the cell. The mean tree heights were calculated only for the model grid cells where the mangrove areas were larger than the half sizes of the cells, and these cells were marked as mangrove cells. It can be seen that tall mangrove trees are mainly distributed along the shoreline, particularly around the mouths of Harney River and Shark River (see Fig. 1 and Fig. 3).

In addition to tree heights, other mangrove characteristics such as stem size and stem density were obtained through allometric equations. For the stem size, while direct allometric relations between tree height and stem diameter are available for mangroves (Tamai et al., 1986; Hirata et al., 2014; Mugasha et al., 2019), they are not specifically targeted at the mangroves in the study area. We therefore derived such equations based on the work of Smith and Whelan (2006) who focused their studies on the mangroves in the study area. Smith and Whelan (2006) suggested the allometric equations between dry biomass and diameter at breast height (DBH) D, and between dry biomass and stem height T for red, black and white mangroves. Thus, the allometric equation between the DBH D and the tree height T can be inferred by eliminating the dry biomass. For the red mangrove (*Rhizophora*

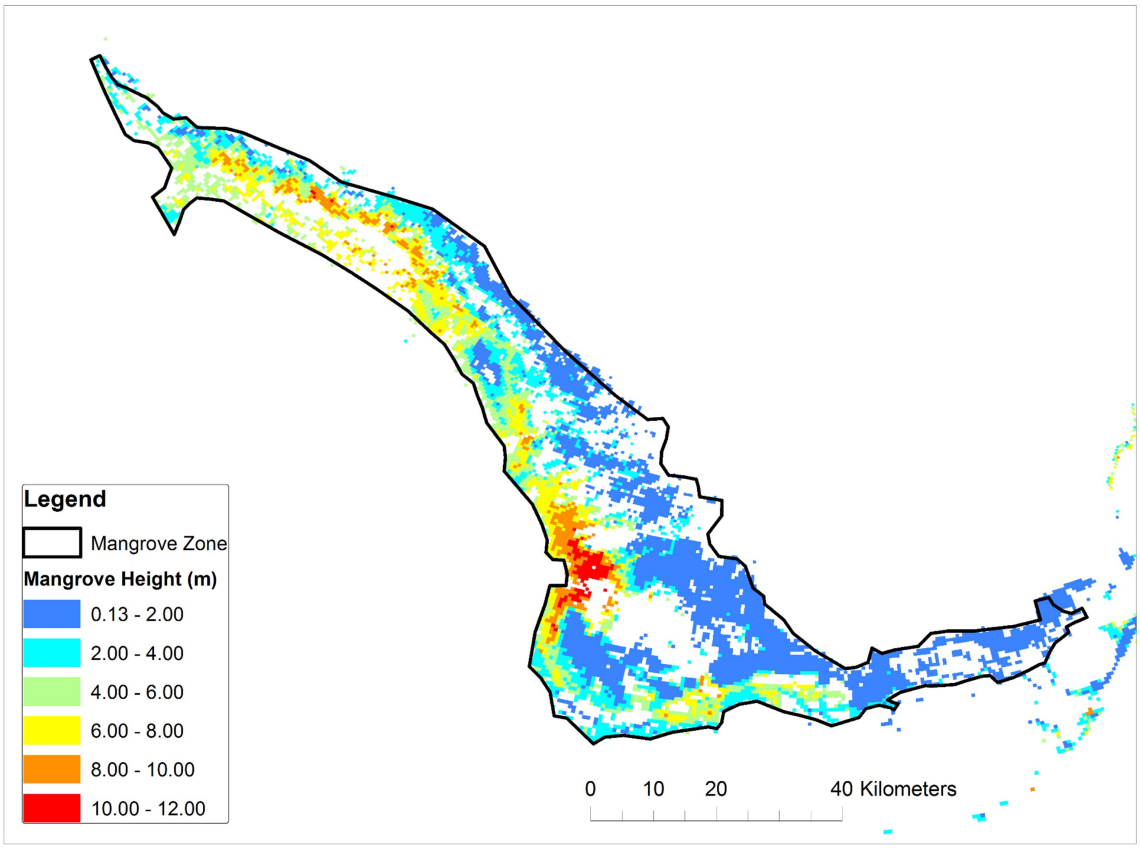

Fig. 3: Map of mean mangrove tree height in the mangrove zone.

mangle) for example, this is expressed as (total variance explained $r^2 \approx 0.93$):

$$D = 10^{\frac{2.357\log_{10} T - 0.657}{1.731}} \tag{1}$$

where the tree height T is in meter (m) and the DBH D is in centimeter (cm). Once the DBH data is available, it is straightforward to calculate the tree density, n, using the equation proposed by Ward et al. (2006) whose data are also based on the South Florida mangrove zone ($r^2 = 0.91$):

$$n = 6.3765 D^{-1.52} \tag{2}$$

where n is the number of trees per square meters and D is in cm.

Species composition is also one of the important characteristics of mangrove tree structures in terms of numerical modeling. Unfortunately, a map of mangrove species composition is yet not available for the study area. A comprehensive vegetation mapping project for the south part of the mangrove zone shows that there are hundreds of unique vegetation classes

within this region, although most of them (around 85%) account for less than 1% of the map (Ruiz et al., 2017, 2018). The most common classes are mangrove forest, mangrove scrub and marsh; these classes together with water account for at least 60% of the region (Ruiz et al., 2017, 2018). It appears that red mangroves, including red mangrove forest, shrubland and scrub, are the dominant vegetation in the southwest part of the mangrove zone where most of the tall trees live (Ruiz et al., 2018), and the red mangrove scrub accounts for a considerably larger portion than any other vegetation in the southeast part (Ruiz et al., 2017). Hence, from the numerical simulation point of view an assumption was made that the characteristics of the trees in the mangrove zone are represented by those of red mangroves; further discussions regarding this assumption are given in Section 6.

3. Incorporation of Red Mangrove in the CEST Storm Surge Model

3.1. Characterization of Red Mangroves

Mangrove trees are complex structures from the perspective of numerical simulation of fluid-structure interaction. Particularly, this paper focuses on the investigation of the attenuation effect of red mangrove on storm surge, which is well known for its tangled prop-roots. It is thus impractical to represent every individual tree with details in the numerical model. An abstract tree model that characterizes the major structural features of red mangrove has to be established in order to enable numerical simulations.

In this study, the red mangrove is characterized into three parts: a leaf-bearing part, a trunk (stem) part and a root part, which are represented by two cylinders and a truncated cone, respectively (see Fig. 4). In addition, based on field observation, the mangroves have been divided into three groups according to the tree height, and each group has different height ratios of the leaf-bearing part and the root part to the trunk part (see Fig. 5). For comparison purpose, photographs taken during a field survey are also displayed in Fig. 5.

Given a tree height T and trunk size D (related by Eq. 1), the characteristic diameters of the leaf-baring part (D_L) and the root part (D_R) shown in Fig. 4 were determined according to two factors: (1) the height ratios (i.e. T_L/T and T_R/T) as shown in Fig. 5; (2) the biomass ratios of the leafing-bearing part to the trunk part, and the root part to the trunk part, respectively. The biomass ratios were obtained from Smith and Whelan (2006); Fig. 6 shows the ratios of the biomasses of different tree components to the total biomass as a function of tree height. Note that for the current study, the branch and the leaf biomasses were combined together as the biomass of the leaf-bearing part. Assuming a constant material density, these biomass ratios can be reinterpreted as volume ratios between the tree parts,

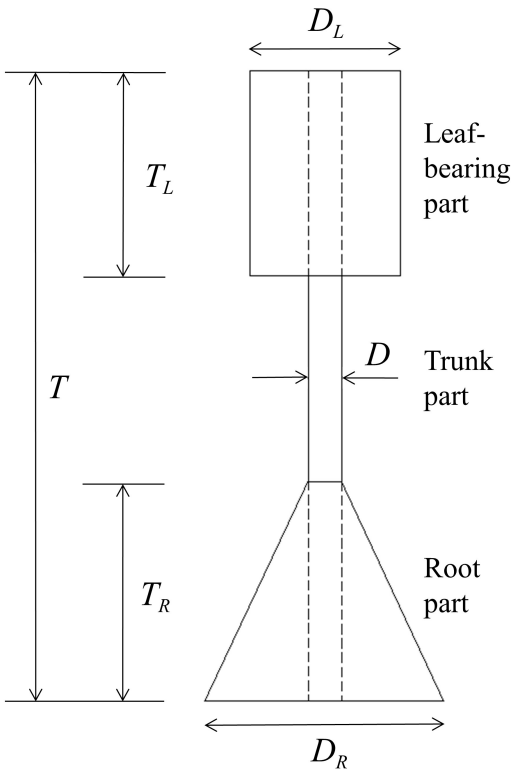

Fig. 4: Sketch showing the simplified structure for red mangrove. The trunk part is represented by a cylinder with diameter D and height T that extends through the whole tree model. The leaf-bearing part and the root part are represented by a cylinder with diameter D_L and height T_L, and a truncated cone with bottom diameter D_R and height T_R, respectively.

which, with the height ratios mentioned above, were used to calculate the values of D_L/D and D_R/D. It is noted that D_L/D and D_R/D determines the shape of the abstract tree model (Fig. 4) and will be seen to be the key parameters in the numerical simulation. Table 1 presents the calculated D_L/D and D_R/D based on a typical tree height in each group. It is found from Table 1 that D_L/D and D_R/D remain almost unchanged as the tree height varies from 1.5 m to 9 m. Hence, in the numerical simulation, D_L/D and D_R/D were fixed at 1.85 and 1.64, respectively, which are the averaged values of those given in Table 1.

3.2. Hydrodynamic Model

The CEST model, in a depth-integrated, two dimensional (2D) form on an orthogonal curvilinear grid was modified to include the mangrove tree component for storm surge modeling. In particular, the mangrove effect is parameterized into a porosity (volume exclusion) coefficient (Wu et al., 2001) and a drag force term (Nepf, 1999); both of these are functions of

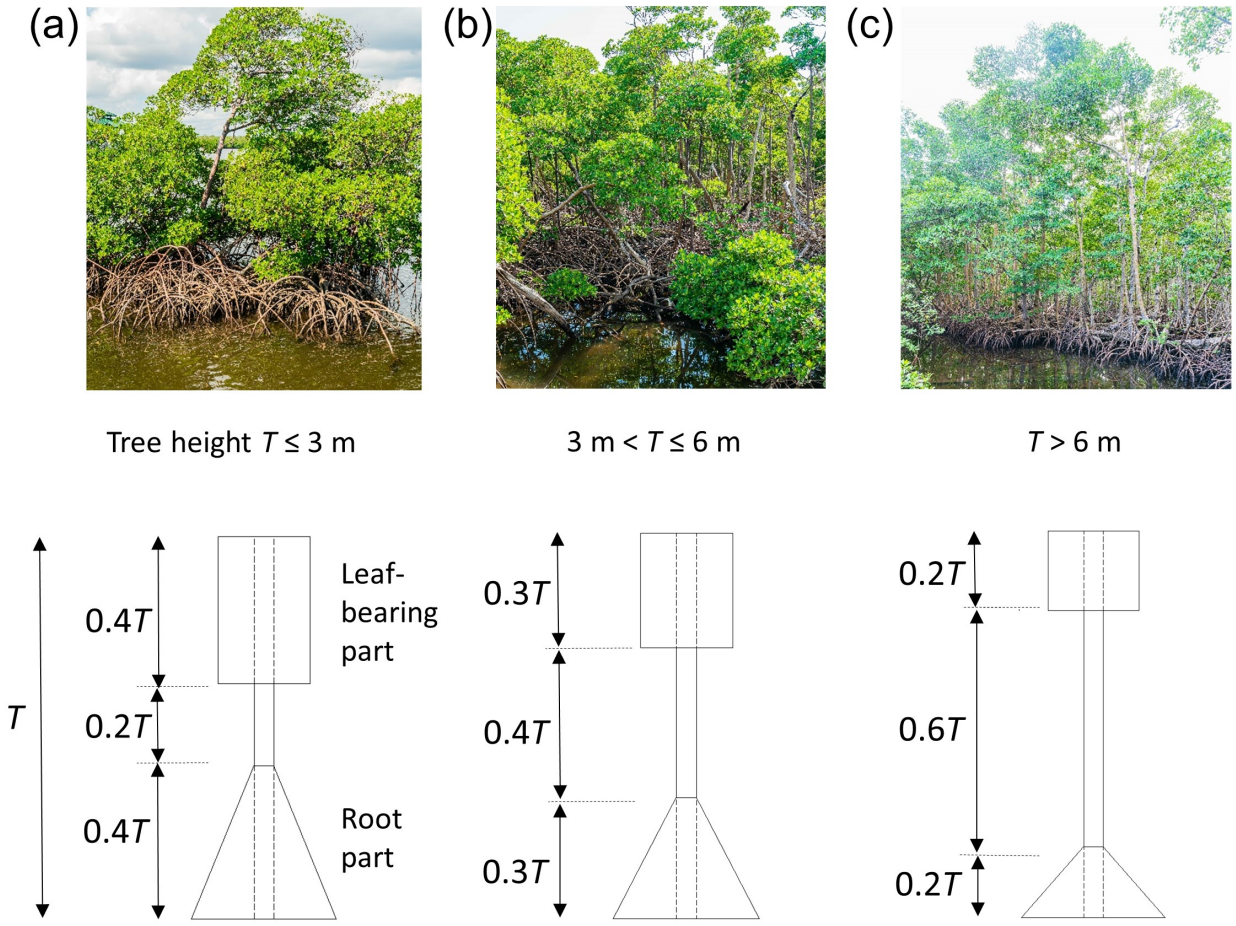

Fig. 5: Sketch showing the grouping of the red mangrove based on the tree height, in contrast with photos taken from field survey.

Table 1: Ratios of D_L/D and D_R/D for typical mangroves in the groups presented in Fig. 5.

Tree height	Leaf-bearing part			Root part		
	Biomass ratio to the trunk part	Height ratio to the trunk part	D_L/D	Biomass ratio to the trunk part	Height ratio to the trunk part	D_R/D
$T = 1.5$ m (in $T \leq 3$ m)	1.024	0.4	1.887	0.323	0.4	1.660
$T = 4.5$ m (in 3 m $< T \leq 6$ m)	0.648	0.3	1.778	0.211	0.3	1.590
$T = 9.0$ m (in $T > 6$ m)	0.513	0.2	1.888	0.161	0.2	1.661

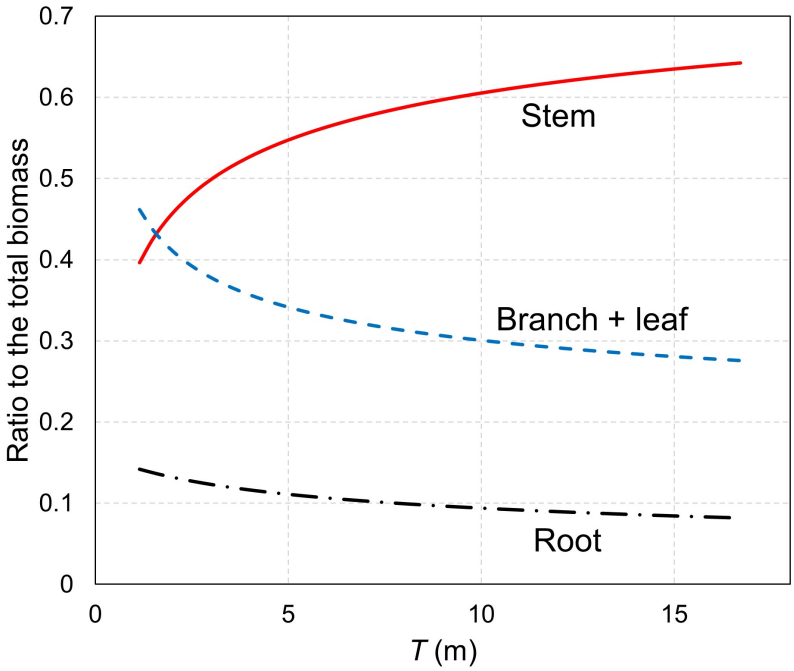

Fig. 6: Biomass ratio of each component to the total biomass as a function of tree height for the red mangrove in the South Florida mangrove zone (data reorganized from Smith and Whelan (2006)).

water depth and the mangrove characteristics. The 2D depth-integrated continuity equation and momentum equations in an x, y, and z coordinate system with z axis perpendicular to the still water level are (Zhang et al., 2012):

$$\frac{\partial \theta H}{\partial t} + \frac{\partial \theta HU}{\partial x} + \frac{\partial \theta HV}{\partial y} = 0 \tag{3}$$

$$\frac{\partial \theta HU}{\partial t} + \frac{\partial \theta HU^2}{\partial x} + \frac{\partial \theta HUV}{\partial y} = f\theta HV - g\theta H\frac{\partial}{\partial x}\left(\zeta + \frac{\Delta P_a}{\rho g}\right) - \frac{F_x}{\rho} - \theta\frac{\tau_b^x}{\rho} + \theta\frac{\tau_s^x}{\rho} + A_h\left(\frac{\partial^2 \theta HU}{\partial x^2} + \frac{\partial^2 \theta HU}{\partial y^2}\right) \tag{4}$$

$$\frac{\partial \theta HV}{\partial t} + \frac{\partial \theta HUV}{\partial x} + \frac{\partial \theta HV^2}{\partial y} = -f\theta HU - g\theta H\frac{\partial}{\partial y}\left(\zeta + \frac{\Delta P_a}{\rho g}\right) - \frac{F_y}{\rho} - \theta\frac{\tau_b^y}{\rho} + \theta\frac{\tau_s^y}{\rho} + A_h\left(\frac{\partial^2 \theta HV}{\partial x^2} + \frac{\partial^2 \theta HV}{\partial y^2}\right) \tag{5}$$

where θ is the porosity coefficient that is defined as the ratio of the water volume versus the total volume of water and mangrove trees on the same area. $H = \zeta + h$ is the overall water depth, h is the water depth from the still water level to the bottom, ζ is the water surface elevation reference to the still water level, U and V are depth-integrated velocities along x- and y- directions respectively, f is Coriolis parameter, g is the gravitational acceleration, ΔP_a is air pressure drop, ρ is the water density, A_h is the horizontal eddy diffusivity, τ_b^x and τ_b^y are the bottom friction forces in x- and y- directions respectively, τ_s^x and τ_s^y are the surface wind stresses in x- and y- directions respectively, and F_x and F_y are the newly added drag forces due to mangroves in x- and y- directions, respectively.

The momentum equations, Eq. 4 and Eq. 5, are further simplified to obtain their non-conservative forms using the continuity equation and the chain rule, and can be written as follows by dividing with θH at both sides:

$$\frac{\partial U}{\partial t} + U\frac{\partial U}{\partial x} + V\frac{\partial U}{\partial y} = fV - g\frac{\partial}{\partial x}\left(\zeta + \frac{\Delta P_a}{\rho g}\right) - \frac{F_x}{\rho\theta H} - \frac{\tau_b^x}{\rho H} + \frac{\tau_s^x}{\rho H} + A_h\left(\frac{\partial^2 U}{\partial x^2} + \frac{\partial^2 U}{\partial y^2}\right) \quad (6)$$

$$\frac{\partial V}{\partial t} + U\frac{\partial V}{\partial x} + V\frac{\partial V}{\partial y} = -fU - g\frac{\partial}{\partial y}\left(\zeta + \frac{\Delta P_a}{\rho g}\right) - \frac{F_y}{\rho\theta H} - \frac{\tau_b^y}{\rho H} + \frac{\tau_s^y}{\rho H} + A_h\left(\frac{\partial^2 V}{\partial x^2} + \frac{\partial^2 V}{\partial y^2}\right) \quad (7)$$

Note that the full diffusion terms, $\frac{A_h}{\theta H}\left(\frac{\partial^2 \theta HU}{\partial x^2} + \frac{\partial^2 \theta HU}{\partial y^2}\right)$ and $\frac{A_h}{\theta H}\left(\frac{\partial^2 \theta HV}{\partial x^2} + \frac{\partial^2 \theta HV}{\partial y^2}\right)$, are simplified to $A_h\left(\frac{\partial^2 U}{\partial x^2} + \frac{\partial^2 U}{\partial y^2}\right)$ and $A_h\left(\frac{\partial^2 V}{\partial x^2} + \frac{\partial^2 V}{\partial y^2}\right)$ following Hervouet et al. (2000). Eq. 3, Eq. 6 and Eq. 7 are the governing equations solved in CEST on an orthogonal curvilinear grid, for which more details can be found in Blumberg and Herring (1987). The equations for τ_s^x, τ_s^y, τ_b^x and τ_b^y, and the handling of wetting and drying process and boundary conditions were given in Zhang et al. (2012).

3.3. Drag Force

In the previous CEST versions (Zhang et al., 2012), the drag force due to land covers was included into the bottom friction term through modifying the Manning coefficient, as both drag force and bottom friction share the same quadratic relationship with flow velocity.

The bed friction in CEST is expressed as:

$$\tau_b^x = C_b \rho \sqrt{U^2 + V^2} U \tag{8}$$

$$\tau_b^y = C_b \rho \sqrt{U^2 + V^2} V \tag{9}$$

$$C_b = \frac{g m^2}{H^{1/3}} \tag{10}$$

where m is the Manning coefficient.

In the current version, the drag forces F_x and F_y due to mangroves are calculated directly, based on the abstract tree models described in Section 3.1 and the landscape scale mangrove data map discussed in Section 2.2. The equations for F_x and F_y are modified from those proposed in Tanaka et al. (2007) and are expressed as:

$$F_x = n \times \int \frac{1}{2} C_{di} \rho u_i \left| u_i \right| \mathrm{d}A_i = \frac{n}{2} \times \alpha \times \overline{C_d} D L \rho U_m \left| U_m \right| \tag{11}$$

$$F_y = n \times \int \frac{1}{2} C_{di} \rho v_i \left| v_i \right| \mathrm{d}A_i = \frac{n}{2} \times \alpha \times \overline{C_d} D L \rho V_m \left| V_m \right| \tag{12}$$

where

$$L = \begin{cases} H & \text{if } H \leq T \\ T & \text{if } H > T \end{cases} \tag{13}$$

where n is the number of trees per square meters, C_{di}, u_i, v_i, $\mathrm{d}A_i$ are the drag coefficient, the velocity in x-direction, the velocity in y-direction and the projected tree area in the ith layer when dividing the tree model (see Fig. 4) vertically into k layers with the same layer height l, D is the DBH, H is the overall water depth, T is the tree height, $\overline{C_d}$ is a bulk drag coefficient representing the mangrove tree array and is set to a constant value of 1.17 according to Nepf (1999), $\mathbf{U}_m = (U_m, V_m)$ is the flow velocity acting on the mangrove and is determined following Stone and Shen (2002):

$$\mathbf{U}_m \approx (L/H)^{1/2} \mathbf{U} \tag{14}$$

where $\mathbf{U} = (U, V)$ is the depth-averaged flow velocity, and α represents the integrated effect of tree structure to the drag force along the water depth.

It is somewhat complicated to calculate α accurately, as it requires the exact details of individual mangrove tree structure. Here, a simplified method is developed based on the abstract tree models (see Fig. 4). As a depth-integrated value, in general, α can be expressed as follows, by dividing the abstract tree model vertically into a number of layers of the same height:

$$\alpha = \frac{1}{L}\int_0^L b(z)\mathrm{d}z \approx \frac{1}{p}\sum_{i=1}^{p} b_i \tag{15}$$

where p is the number of layers under water, b_i is an amplification factor of the projected tree area at the ith layer to that at the DBH layer, which accounts for an increase of the drag force due to mangrove roots, branches or leafs, in addition to that provided by the mangrove trunk. To calculate b_i, here an assumption is made that at each layer in the root part, the abstract tree model can be further divided into a number of small cylinders representing the prop-roots of red mangrove, plus a cylinder representing the trunk; the prop-root cylinders are assigned with an identical diameter equal to X and a height equal to the layer height, and the trunk cylinder has the same diameter as DBH and also a height equal to the layer height (see Fig. 7). As such, b_i can be computed as:

$$b_i = \frac{(D + q_i X)\, l}{Dl} \tag{16}$$

where q_i is the number of the prop-root cylinders at the ith layer, D is the DBH, and l is the layer height. To calculate q_i, the shape of the ith layer abstract tree model is also simplified into a cylinder (see Fig. 7), given a very small layer height (namely a large number of layers). Thus, q_i can be expressed as:

$$q_i = \frac{D_i^2 - D^2}{X^2} \tag{17}$$

where D_i is the diameter of the abstract tree model at the ith layer, which based on Fig. 4 is calculated as:

$$D_i = \begin{cases} D_R - (D_R - D)L/T_R & \text{if } L \le T_R \\ D & \text{if } T_R < L \le T - T_L \\ D_L & \text{if } T - T_L < L \le T \end{cases} \tag{18}$$

where T_R and T_L are the heights of the root part and the leaf-bearing part of the abstract

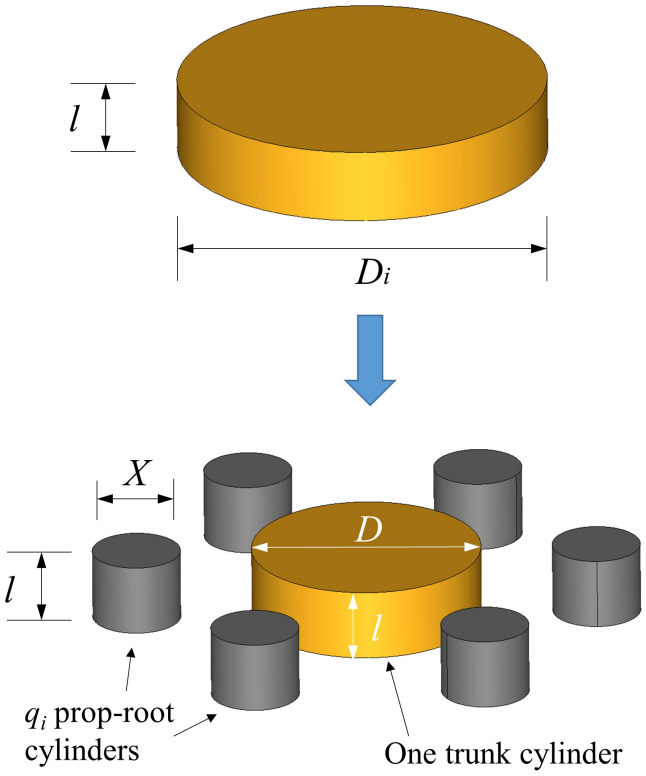

Fig. 7: Schematic showing the idea of further dividing one layer (the ith layer) of the abstract tree model into one trunk cylinder and q_i prop-root cylinders in a volume conservative manner.

tree model, respectively. Finally, by inserting Eq. 17 into Eq. 16, b_i is obtained as:

$$b_i = 1 + \frac{D_i^2 - D^2}{XD} \tag{19}$$

It is clear from Eq. 19 that a larger X will give a smaller b_i. As an estimation, in the current study X is given half the trunk diameter, i.e. $D/2$. However, statistical data for X from field study by ecological researchers would improve the accuracy of the current model. Note that Eq. 19 is also used at the leaf-bearing part of the abstract tree model in the same manner, approximating the effect of tree branches and leaves on the drag force. Finally, in the current study a total number of 100 layers are used to vertically divide the abstract tree models, and Fig. 8 shows the calculated value of α for the three group of mangrove trees listed in Fig. 5.

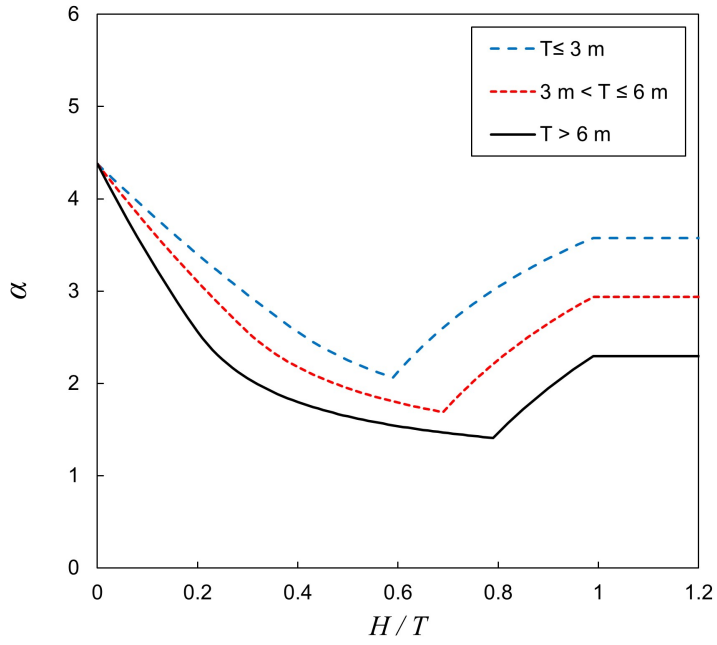

Fig. 8: Value of α as a function of water depth, accounting for a depth-averaged increase of the drag force due to the root, branch and leaf of red mangrove.

3.4. Porosity Coefficient

In the literature, very few papers have presented relevant data in terms of mangrove porosity as a function of water depth. For example, Mazda et al. (1997) suggested such data for *Rhizophora stylosa* (red mangrove) and *Bruguiera gymnorhiza* (black mangrove) located in islands in Japan and Australia up to a water depth of only 0.5 m. However, strong storms could cause water of several meters high (Zhang et al., 2012). The tree model proposed in this paper (see Fig. 4) provides an easy access to the calculation of the porosity coefficient. The idea is a simple one: the volume of mangrove tree, V_M, at different water depths can be calculated by:

$$V_M = \gamma V_C \tag{20}$$

and

$$V_C = \frac{\pi L D^2}{4} \tag{21}$$

where V_C is the trunk part cylinder volume at depth L, which makes γ an amplification coefficient due to the additional root, branch and leaf of mangroves. Similar to Eq. 15, it is

trivial to obtain the expression for γ:

$$\gamma = \frac{1}{L}\int_0^L c(z)\mathrm{d}z \approx \frac{1}{p}\sum_{i=1}^{p} c_i = \frac{1}{p}\sum_{i=1}^{p}\frac{\mathrm{d}V_i}{\mathrm{d}V_{\mathrm{DBH}}} = \frac{1}{p}\sum_{i=1}^{p}\left(\frac{D_i}{D}\right)^2 \tag{22}$$

where c_i is the volume amplification coefficient for the ith layer, $\mathrm{d}V_i$ and $\mathrm{d}V_{\mathrm{DBH}}$ are the volume of mangrove tree model at the ith layer and at the DBH layer, respectively, D_i is the diameter of the abstract tree model at the ith layer (see Eq. 18). Fig. 9 presents the calculated value of γ used in the numerical simulations.

Finally, the porosity coefficient θ considering the structural characteristics of red mangrove and the water depth is expressed by:

$$\theta = 1 - \frac{(n\Delta x\Delta y)V_M}{H\Delta x\Delta y} = 1 - n\frac{\pi D^2 L}{4H}\gamma_L \tag{23}$$

where γ_L is the γ value at the water depth of L. According to the above equation, it was found that the porosity coefficient is in general close to 1, implying that the volume ratio of mangrove to the total volume on the same area is very low. As an example, assuming that the water depth is very low such that $L = H$ (see Eq. 13) and γ_L is equal to the maximum value of γ as seen in Fig. 9, the value of θ is found to decrease from 0.9986 to 0.9948 when the tree height varies from 2 m to 15 m.

4. An idealized test case

In this section, an idealized test case, concerning the simulation of storm surge onto an idealized coastal plain planted with red mangroves, is designed to examine the characteristics of the proposed method. These mainly include the importance of the porosity term at different scenarios and the difference between the current method and the Manning coefficient based method in terms of modeling mangrove resistance to water flows during storm surge impact.

4.1. Setup of the test case

Fig. 10 shows the computational basin for the idealized test case. The ground elevation is set to be similar to natural bathymetry ranging from very deep water in the ocean basin to very shallow water in the continental shelf. The ground elevation for the entire coastal plain, i.e. the land area shown in Fig. 10, is fixed at the still water level, which is attempted to minimize the effect of topography on storm surge. The land area is designated as the

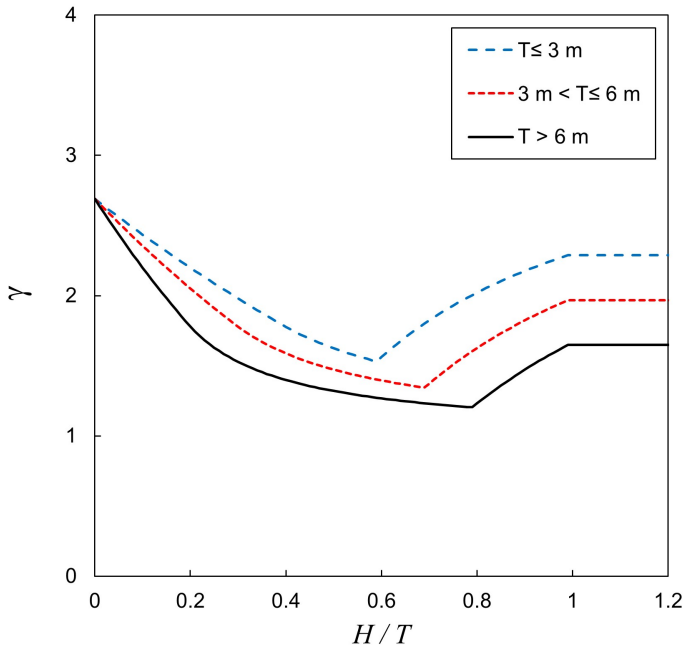

Fig. 9: Value of γ as a function of water depth, accounting for a depth-averaged increase of the volume of red mangrove due to its root, branch and leaf.

mangrove zone, where the mangrove tree data for the current method are set following the allometric equations as needed. The hurricane for the idealized test case is designed based on Hurricane Wilma (2005). All of the features of Wilma's track were employed and a similar landfall location was maintained (see Fig. 1 and Fig. 10), except that the atmosphere pressure is slightly modified to generate three hurricanes that will lead to different storm surge severities. In other words, the three hurricanes, named as Hurricane 1, 2 and 3, share the same track shown in Fig. 10 but have different central pressure values close to landfall. The wind field was computed by using the parametric wind model employed by the SLOSH (Sea, Lake, and Overland Surges from Hurricanes) model (Jelesnianski et al., 1992). Table 2 gives the input parameters of the SLOSH wind model at the locations marked in Fig. 10, including the radius of maximum wind (RMW), maximum wind speed (MWS), and central pressure. As an example, Fig. 11 shows the computed peak surge heights for the three hurricanes, where the mangrove tree characteristics are set to $T = 6.5$ m, $D = 0.053$ m and $n = 0.5$ according to Eq. 1 and Eq. 2. As expected, Hurricane 1 leads to the smallest storm surge and Hurricane 3 results in the largest one. Finally, the grid size is set to approximately 1700 m $\times$ 1700 m in the deep ocean area and 350 m $\times$ 350 m near the shoreline, with the total number of grid cells being nearly 470,000. The simulated time is 2 days with a time step of 10 seconds for each of the simulations presented in this section.

Table 2: Parameters for the SLOSH wind model.

Location	Time (hours)	RMW (km)	MWS (km/h)	Central pressure (hPa)		
				Hurricane 1	Hurricane 2	Hurricane 3
#1	0	64.4	144.0	963	963	963
#2	12	77.2	157.7	963	933	903
#3	18	119.1	125.2	960	930	900
#4	21	121.8	123.5	962	932	902

Table 3: Parameters for testing the effect of the porosity term.

Group	Hurricane	Mangrove		
		Height T (m)	Diameter D (m)	Density n (m^{-2})
1	1, 2, 3	3.0	0.019	2.5
2	1, 2, 3	4.5	0.032	1.1
3	1, 2, 3	6.5	0.053	0.5

4.2. Importance of the porosity (volume exclusion) term θ

The porosity term represents the fact that mangroves occupy part of the water volume during storm surge. Theoretically, when the porosity approaches zero (i.e. there is no water), the mangroves will act like a 'wall', and when the porosity approaches one (i.e. there is no mangrove), the effect of the porosity term will vanish. It is therefore interesting to investigate the effect of the porosity term for the mangroves abstracted under the current numerical framework.

As demonstrated in Section 3.4, the ratio of mangrove volume to the total volume of water and mangrove on the same area is, in general, very low. In the literature, some researchers have argued that the effect of the porosity is negligible when the volume of vegetation is low (Wu et al., 2001; Wu and Marsooli, 2012); however, their work was not undertaken within the context of storm surge, nor were the mangrove tree characteristics considered. Here, three group of tests were conducted; their parameters are given in Table 3. In each group, the tree height was first selected and then the trunk diameter and the density were calculated using Eq. 1 and Eq. 2. Note that the tree height setup for each group leads to the use of the different tree models listed in Fig. 5. The effect of the porosity term is assessed by comparing the maximum storm surge heights along profile A-B (see Fig. 10).

Fig. 12 shows the computed peak surge profiles with and without the porosity effect (by enforcing $\theta = 1$ in every wet cell). It is obvious that for all of the tree sizes and the hurricane intensities, the results run with and without the porosity effect are indistinguishable. Thus, in the current study the effect of the porosity term on mangrove resistance to storm surge

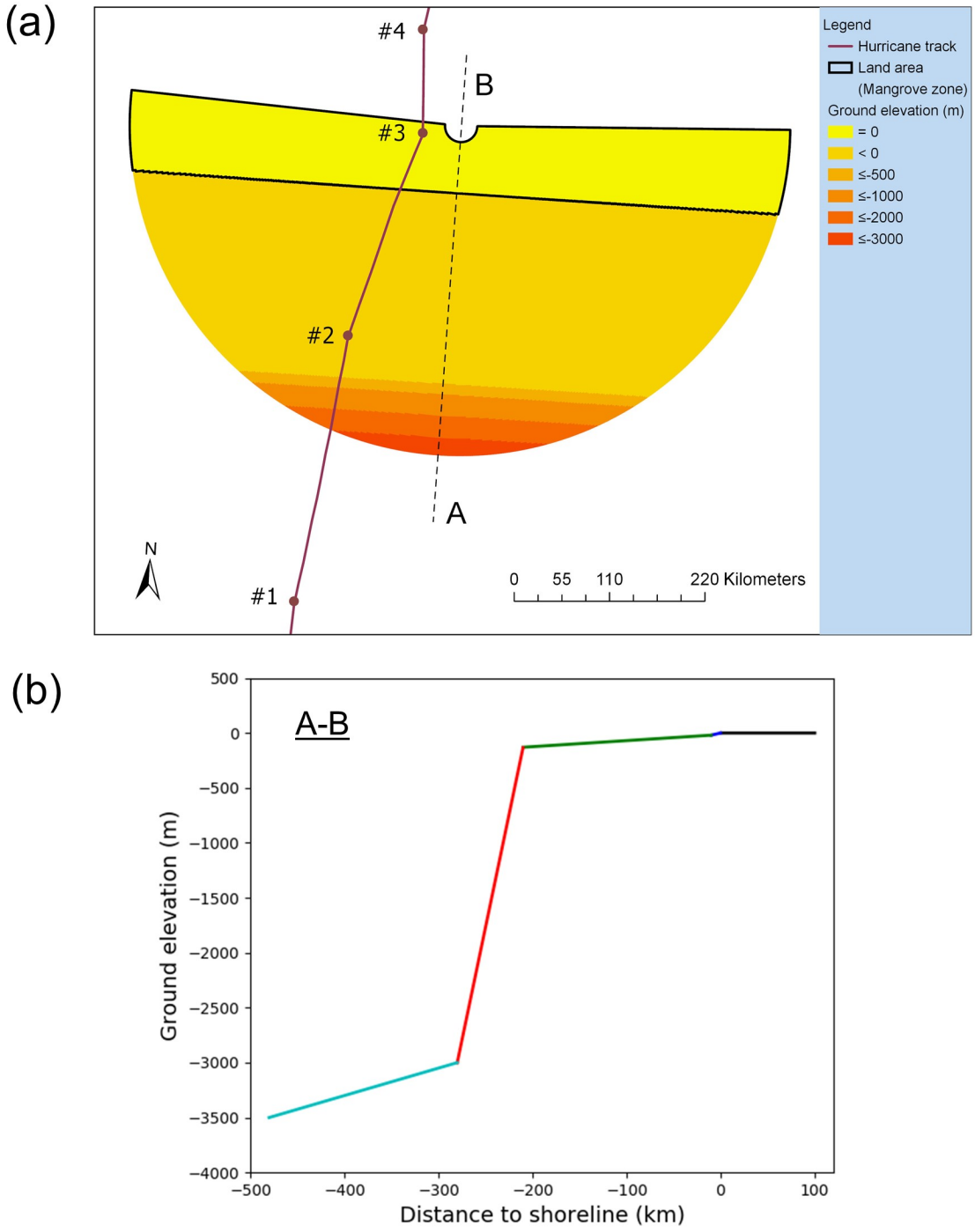

Fig. 10: The computational basin for the idealized test case. (b) shows the detailed ground elevation for profile A-B depicted using the dashed line in (a). The value of ground elevation is referenced to the still water level. The hurricane travels from the south to the north.

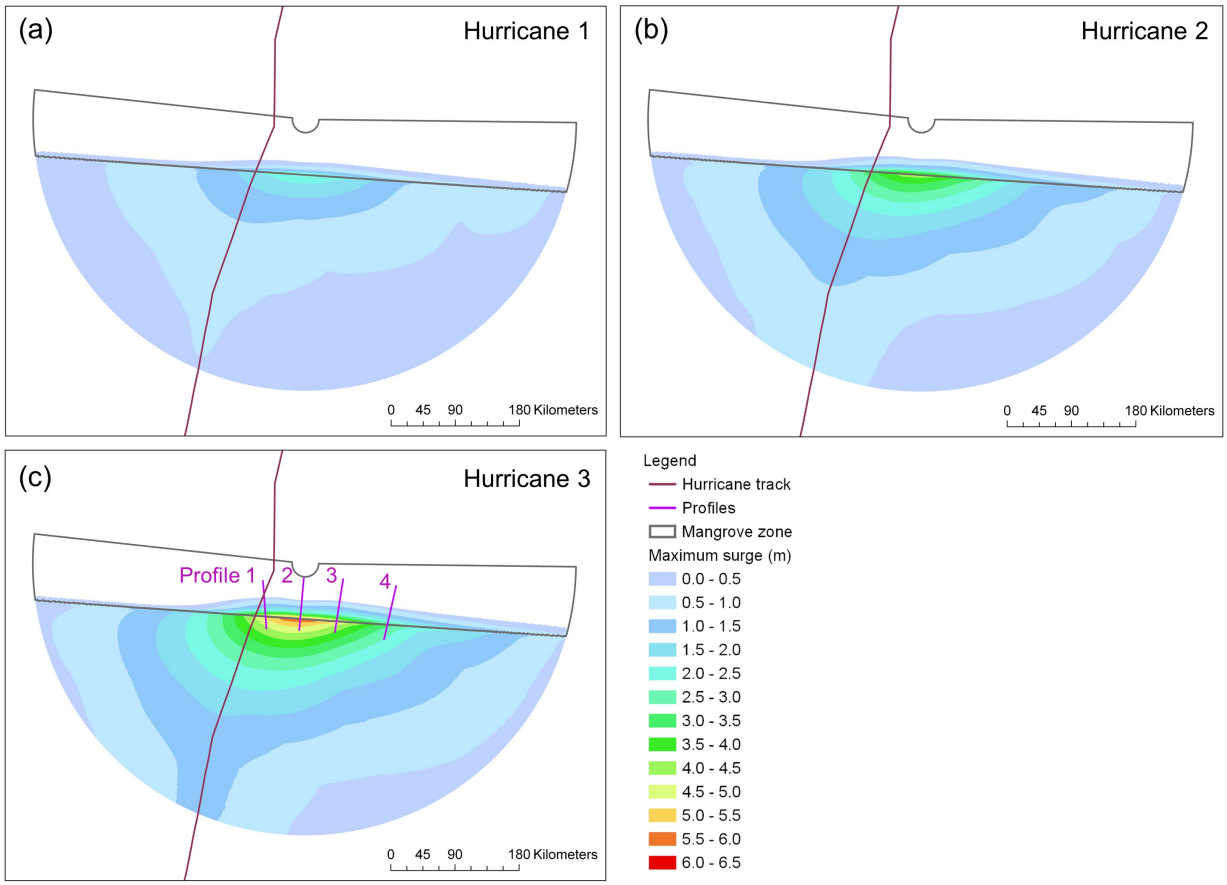

Fig. 11: Computed peak surge heights for the three hurricanes using the current porosity plus drag force method. The mangrove tree data are $T = 6.5$ m, $D = 0.053$ m and $n = 0.5$.

is negligible, which is due likely to that in general, the porosity term θ is close to 1.0 as seen from the calculations in Section 3.4. Meanwhile, it is interesting to notice that the relatively short tree ($T = 3.0$ m) appears to generate shorter inundation distances when compared with the tall tree ($T = 6.5$ m) at the same hurricane conditions; the reason for this is discussed in the following section.

4.3. Comparison between the current method and the Manning coefficient method

The Manning coefficient method has been successfully employed for modeling mangrove effect on storm surge attenuation (Zhang et al., 2012; Xu et al., 2010; Liu et al., 2013). It typically requires an empirical value of the Manning coefficient to account for the mangrove effect. In contrast, in the current method the mangrove tree characteristics are considered in a more physical manner. This section gives more in-depth comparisons between the two

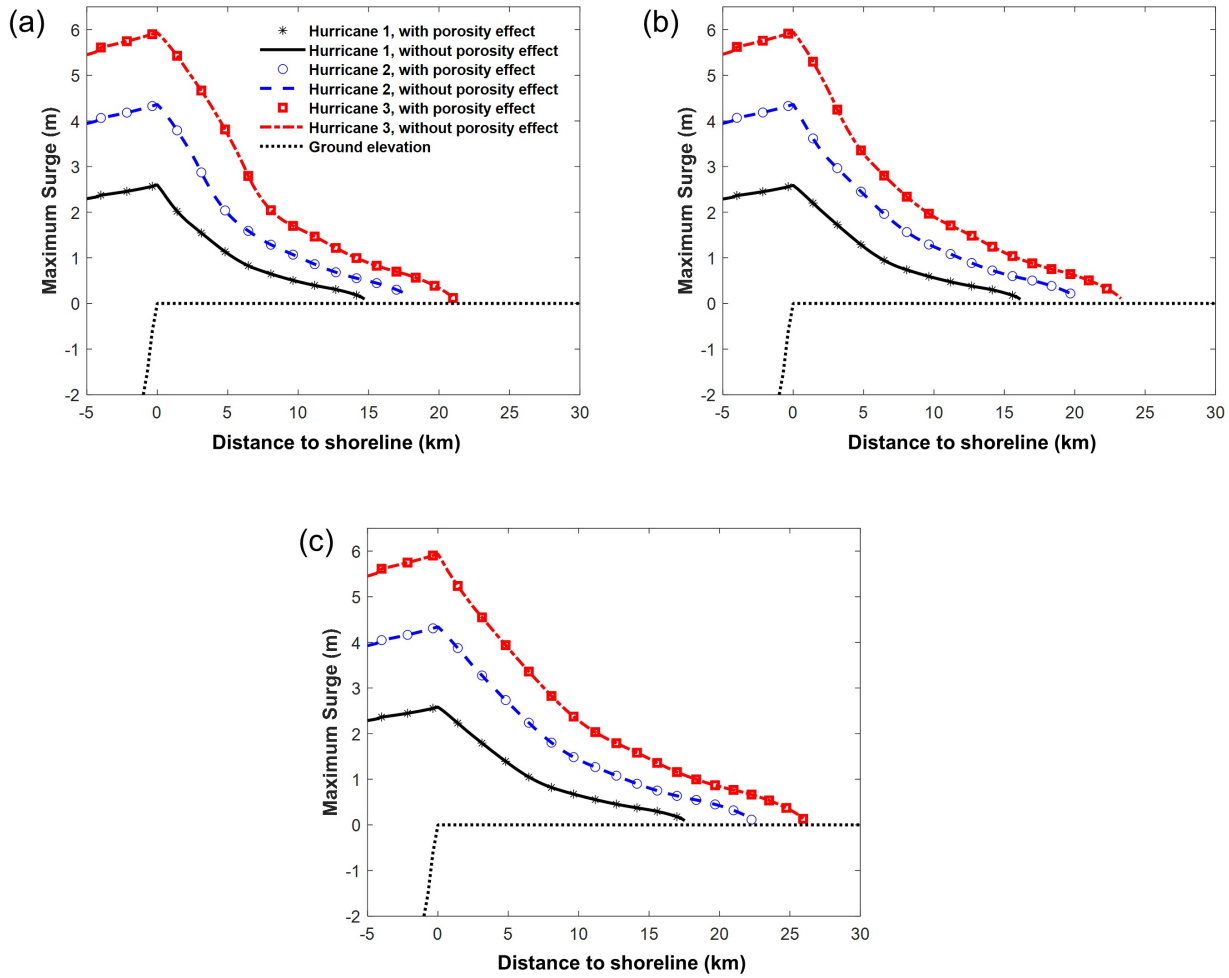

Fig. 12: Comparison for the computed peak surge heights along profile A-B (see the profile location in Fig. 10) between results run with and without the porosity effect. Three typical tree sizes are tested and each of them is impacted by the three hurricanes: (a) $T = 3.0$ m, $D = 0.019$ m, $n = 2.5$, (b) $T = 4.5$ m, $D = 0.032$ m, $n = 1.1$, and (c) $T = 6.5$ m, $D = 0.053$ m, $n = 0.5$.

methods. Hereafter, the current method is referred to as the Porosity plus Drag Force (PDF) method in contrast to the Manning coefficient based Bottom Friction force (MBF) method.

Since it has been shown that the porosity term is insignificant in the previous section, the drag force term due to the PDF method and the bed friction term owing to the MBF method are the key factors in determining the difference between the two methods. Recalling the drag force term and the bed friction term in the x-direction momentum equation (Eq. 6) for example, we have:

$$\frac{F_x}{\rho\theta H} = \frac{n\alpha\overline{C_d}DL}{2\theta H}U_m\left|U_m\right| \approx \frac{n\alpha\overline{C_d}D}{2\theta}\left(\frac{L}{H}\right)^2 U\left|U\right| \tag{24}$$

$$\frac{\tau_b^x}{\rho H} = \frac{gm^2}{H^{4/3}}\sqrt{U^2+V^2}U \tag{25}$$

Ignoring the velocity quadratic term, the difference between the two methods is in fact down to the coefficients $\frac{n\alpha\overline{C_d}D}{2\theta}\left(\frac{L}{H}\right)^2$ and $\frac{gm^2}{H^{4/3}}$, where θ can be further set to 1. Let the Manning coefficient m be 1.4 for the mangroves following Zhang et al. (2012), Fig. 13 plots the two coefficients as a function of water depth for comparison. It is seen from Fig. 13 that the coefficient for the MBF method decreases monotonically as the water depth increases, while the curves for the PDF method show a consistent pattern of decreasing, increasing, and decreasing. For the MBF method, this trend is due to the coefficient being inversely proportional to the water depth. For the PDF method, however, the coefficient is also a function of mangrove tree characteristics; in general, as the water depth increases, the initial high drag force due to the root part of the red mangrove decreases, then it increases back when the water depth reaches the leaf-bearing part, and finally when the tree is submerged, the drag force decreases again as the water depth continues to rise. For the PDF method, at least two conclusions can be drawn: 1) when the water depth is less than 2 m, shorter trees cause a larger coefficient, and when the water depth increases, this trend is slowly altered to the opposite; 2) the coefficients for different tree heights converge to a small value as the water depth becomes very large ($>$ 8 m). Comparing the two coefficients, in general, the MBF method related coefficient is significantly larger than that related to the PDF method when the water depth is smaller than 1 m, regardless of the tree height. When the water depth is larger than 1 m, the PDF method related coefficient starts to exceed that of the MBF method at a critical water depth that varies and is in general larger for taller trees. However, it is noted that the MBF method coefficient should be larger than any of the PDF method coefficient at extremely large water depth, because the former is proportional to $H^{-4/3}$ while the latter is proportional to H^{-2} (see e.g. $T = 2$ m in Fig. 13).

Fig. 14 presents comparison for the computed peak surge profiles between the results run using the MBF and the PDF methods, where the tree height $T = 6$ m is selected for simulation. For the case selected, when the water depth is less than 4 m, the MBF method coefficient is larger than the PDF method coefficient (see Fig. 13), which means the MBF method predicts a higher mangrove resistance to the water flow, and the situation transposes when the water depth is larger than 4 m. This trend is clearly reflected in the computed profiles. For example, at Profile 2 where Hurricane 3 leads to a maximum surge of approximately 6 m, the decay rate of the computed peak surge profile by the PDF method is larger than that by the MBF method within 7 km extend to the shoreline, where the

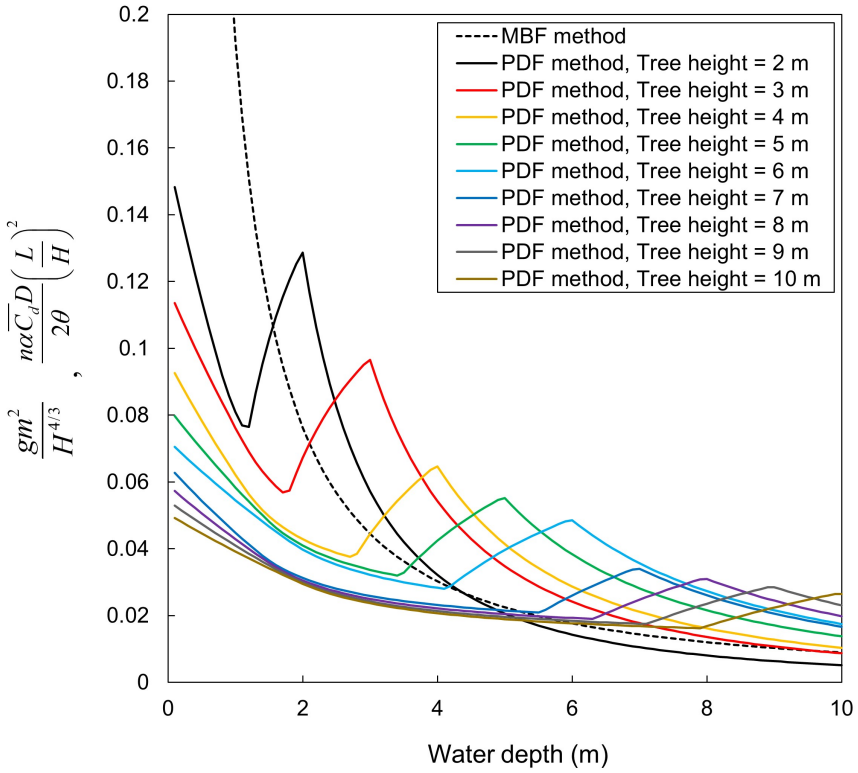

Fig. 13: Comparison between the key coefficients of the drag force term (the PDF method) and the bed friction term (the MBF method).

water depth is in general larger than 4 m during the passing of the storm surge peak. On the contrary, at Profile 4, where the maximum surges due to the three hurricanes are all less than 4 m, the MBF method predicts in all cases a higher decay rate when compared to the PDF method.

Similarly, according to Fig. 13, the drag force related coefficient for $T = 6.5$ m can be expected to be smaller than that for $T = 3.0$ m in the water depth range of 0 to 6 m; this explains the point raised in the previous section that the short mangrove trees outperform the tall mangrove trees on reducing the inundation extend of storm surge, despite some short-period submergence of the short trees.

5. Storm Surge of Hurricane Wilma (2005)

To verify the PDF method, this section focuses on the numerical modeling of the real-world storm surge due to Hurricane Wilma (2005).

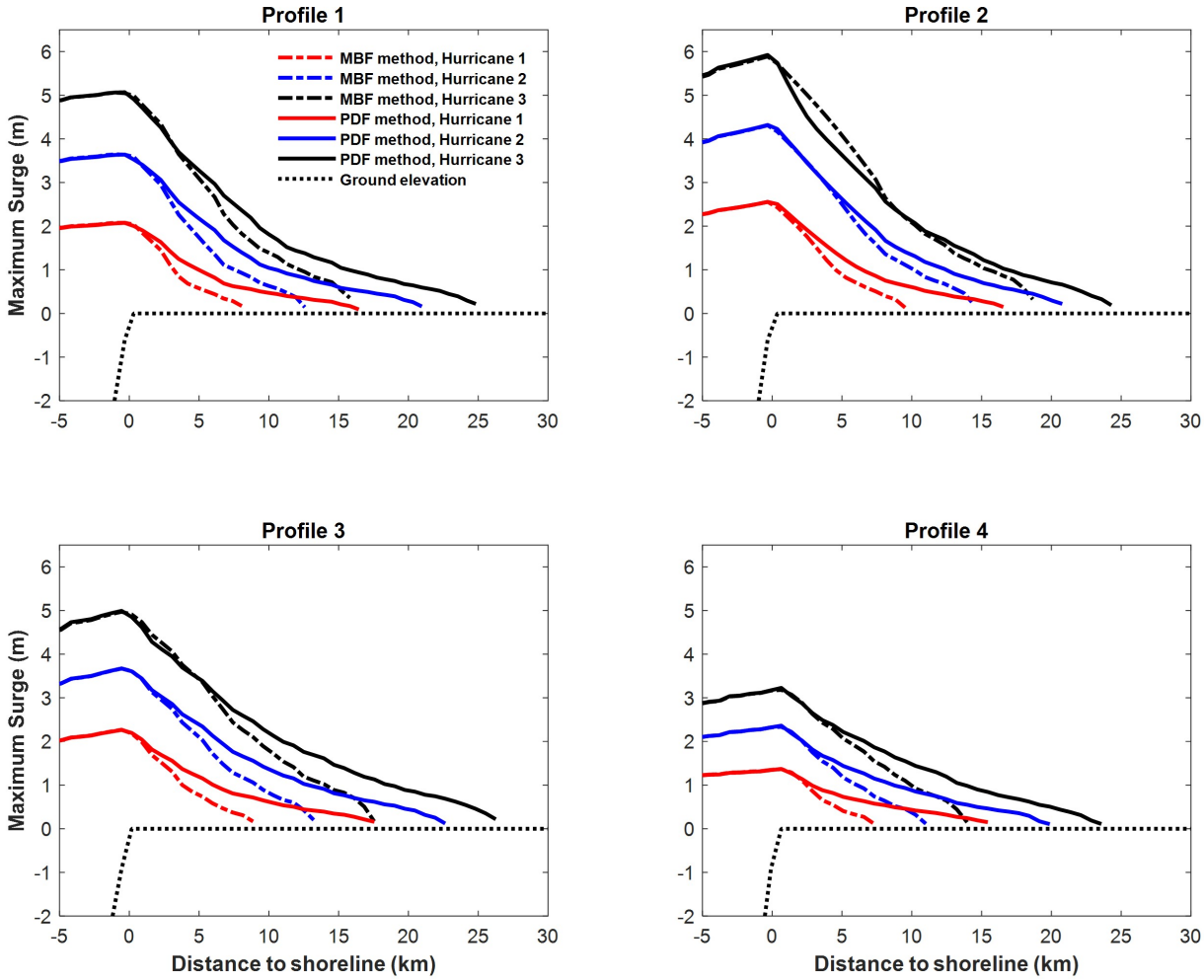

Fig. 14: Comparison for the computed peak surge heights along the four profiles depicted in Fig. 11(c) between results run by the MDF method (Manning coefficient set to 1.4) and the PDF method ($T = 6.0$ m, $D = 0.048$ m and $n = 0.6$).

5.1. Model Setup

This test case was previously investigated by Zhang et al. (2012) and Liu et al. (2013) using the CEST model. In their work, the effect of land cover was accounted for via bottom friction, which was calculated using an enhanced Manning coefficient map. The Manning coefficient changes spatially according to the type of the land cover. In particular, the Manning coefficient for mangroves was set to a constant value of 0.14. In this work, in addition to the drag force, a background Manning coefficient of 0.02 is used in the calculation of the bed friction on the ground in the mangrove zone where computational cells are marked as containing mangroves. When the mangroves are submerged, the extra bed friction on the

top of the mangroves is ignored in comparison with the drag force exerted by the mangroves. For model grid cells that are not marked as mangrove cells, no drag force or mangrove porosity is considered, and only bottom frictions (due to other land covers) are applied based on the enhanced Manning coefficients (Zhang et al., 2012). Simulation results based on these setups are again referred to as the PDF method results. For comparison purpose, simulations employing the same Manning coefficient method as that by Zhang et al. (2012) for modeling mangroves are also conducted, and those are referred to as the MBF method cases as previous. Each simulation continued for 8 days with a time step of 10 s, starting at 18:00 UTC on 20th October 2005 and ending at 18:00 UTC on 28th October.

The Sea, Lake, and Overland Surges from Hurricanes (SLOSH) model grid (Jelesnianski et al., 1992), covering about 400,000 km^2 area of ocean and land in South Florida (Fig. 1), is converted into a CEST grid for storm surge simulation following the procedure developed by Zhang et al. (2013). The CEST model can run on the conformal SLOSH grid without changing the geometries of the model domain and grid cells. The SLOSH grid was developed by National Hurricane Center of NOAA for modeling storm surges and establishing evacuation zones in South Florida. The SLOSH grid consists of about 640,000 cells and the grid size is approximately 450×450 m along the coastal area in the study site and 1500×1500 m in the open ocean. The water depths and elevations of SLOSH grid cells were computed using most recent ETOP1 global bathymetric data set, coastal relief data sets, and LiDAR data sets for Florida. The major river channels and topographic barriers which affect inland inundation of storm surges were incorporated into the model domain through sub-grid features such as flows, cuts, and barriers (Jelesnianski et al., 1992).

The water levels at the open boundary are generated using seven tidal constituents M2, S2, N2, K1, O1, K2, and Q1, which are obtained from the U.S. Army Corps of Engineers (USACE) East Coast 2001 database of tidal constituents (Mukai et al., 2002). The wind field computation employs the H*Wind data, generated by NOAA based on field measurements (Powell et al., 1998), and when H*Wind data are not available, the parametric wind model used by SLOSH is used. For details of the wind field computation in CEST, including terrain effect on the wind, the reader is referred to Zhang et al. (2012).

5.2. Simulation results of Hurricane Wilma (2005)

Fig. 15 shows the distribution of the computed peak surge heights within the whole computational domain using the PDF method (Fig. 15a) and the MBF method (Fig. 15b), respectively. The maximum surge heights are around 4.3 m from both methods and occur at the center of the mangrove zone between Chatham River and Shark River (see Fig. 1 and

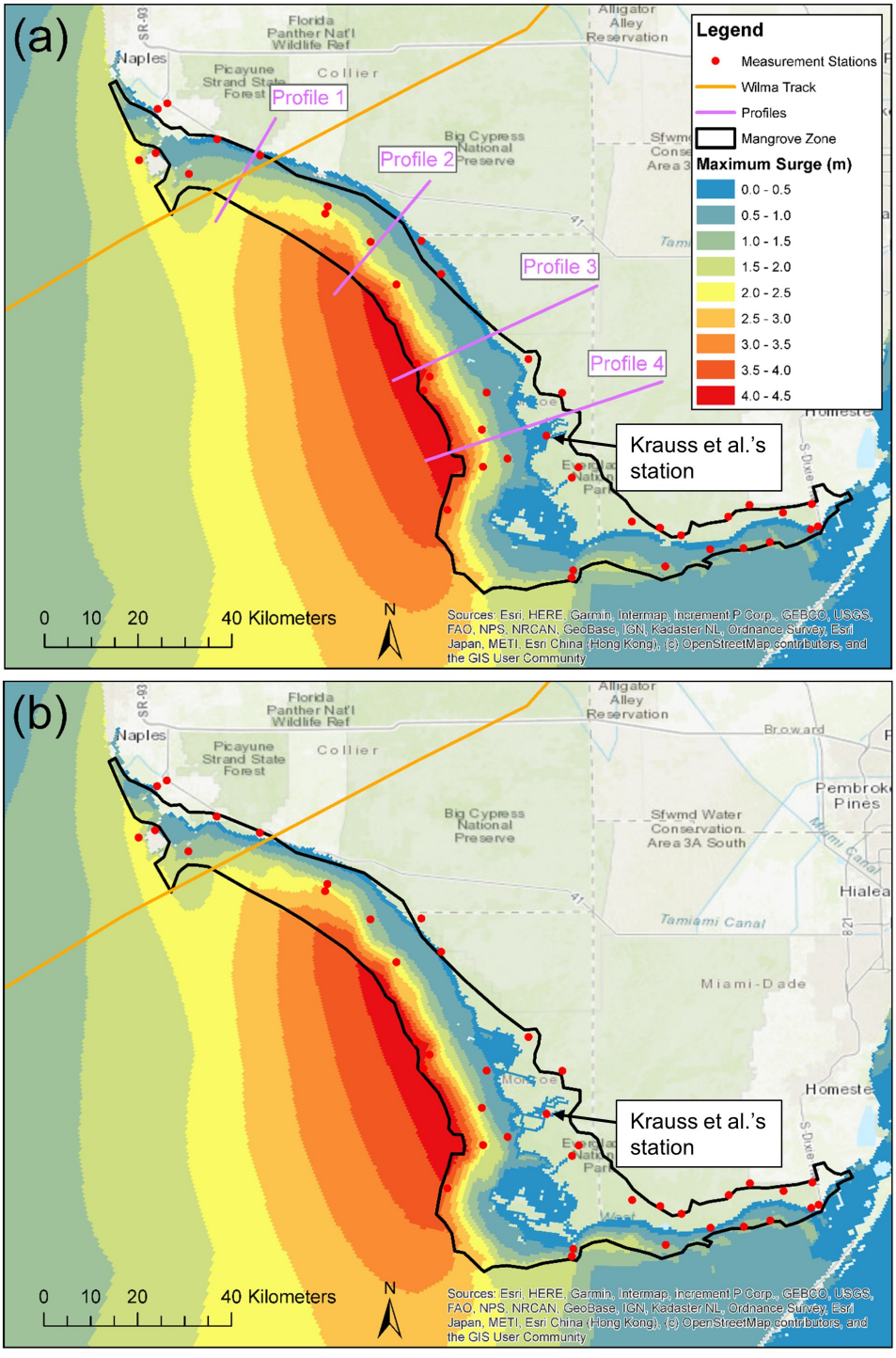

Fig. 15: Computed peak surge heights using the PDF method (a) and the MBF method (b). The location of the four profiles in Fig. 16 is also depicted in (a). The red dots represent the measurement stations shown in Fig. 1.

Fig. 15), which are consistent with the field survey measurements from Smith et al. (2009). However, the PDF method generates a larger inundation area (approximately 350 km^2 more) across the mangrove zone when compared with that obtained by the MBF method, and more measurement stations, located further inland and experienced the storm surge caused by Wilma (2005), are covered by or closer to the edge of the simulated storm surge from the PDF method. It is worth noting that the water level recorder from Krauss et al. (2009) (see Fig. 15) was deployed inland 50 to 80 m from the river's edge and located at 18.2 km upstream of the Shark River; the MBF method produces storm surges only inside the rivers at such long distance, while the PDF method predicts an inundation area covering Krauss et al.'s inland station (see Fig. 15). Based on these observations, it appears that the PDF method produces an improved result for the surge inundation extent compared with the MBF method (further confirmed by the HWM comparison in Fig. 17).

The difference between the computed peak surge heights by the two methods is shown clearly along four profiles in Fig. 16 (profile location is given in Fig. 15a). Results run without the mangrove effect (i.e. $F_x = F_y = 0$) are also plotted for comparison. The PDF method predicts inundation extents 1.5 km to 3.0 km longer than those obtained by the MBF method. However, the maximum surge heights at the front of the mangrove zone are similar for both methods, and increased by 15%-30% compared to those computed without the mangrove effect. The PDF method derives, on average, a decay rate of the peak surge heights of approximately 18 cm/km across the areas with a mixture of mangrove islands and open water (Profiles 1 and 2) and nearly 24 cm/km through dense mangrove forest areas (Profiles 3 and 4). The corresponding rate predicted by the MBF method are 22 cm/km and 29 cm/km, respectively. Note that the decay rate was calculated using the peak surge heights at the front and the back of the mangrove zone (or the inland end of the inundation if the surge remains inside the mangrove zone), and the effect that the surge amplitude decreases as it moves inland even without mangroves was not excluded.

Fig. 17 and Fig. 18 present the comparisons between the simulated and the observed results for the HWMs and the time series of water levels at both river stations and NOAA tide gauges (see Fig. 1 for station location), respectively. The computed HWMs from both the PDF method and the MBF method match well with the observations (Fig. 17). The root mean square errors (RMSEs) of the simulated results against the observation data for the PDF and the MBF methods are 0.43 and 0.45, respectively, which confirms the better performance of the PDF method. Nevertheless, the comparison not only verifies the PDF method but also hints that the Manning coefficient of 0.14 for mangroves as suggested by

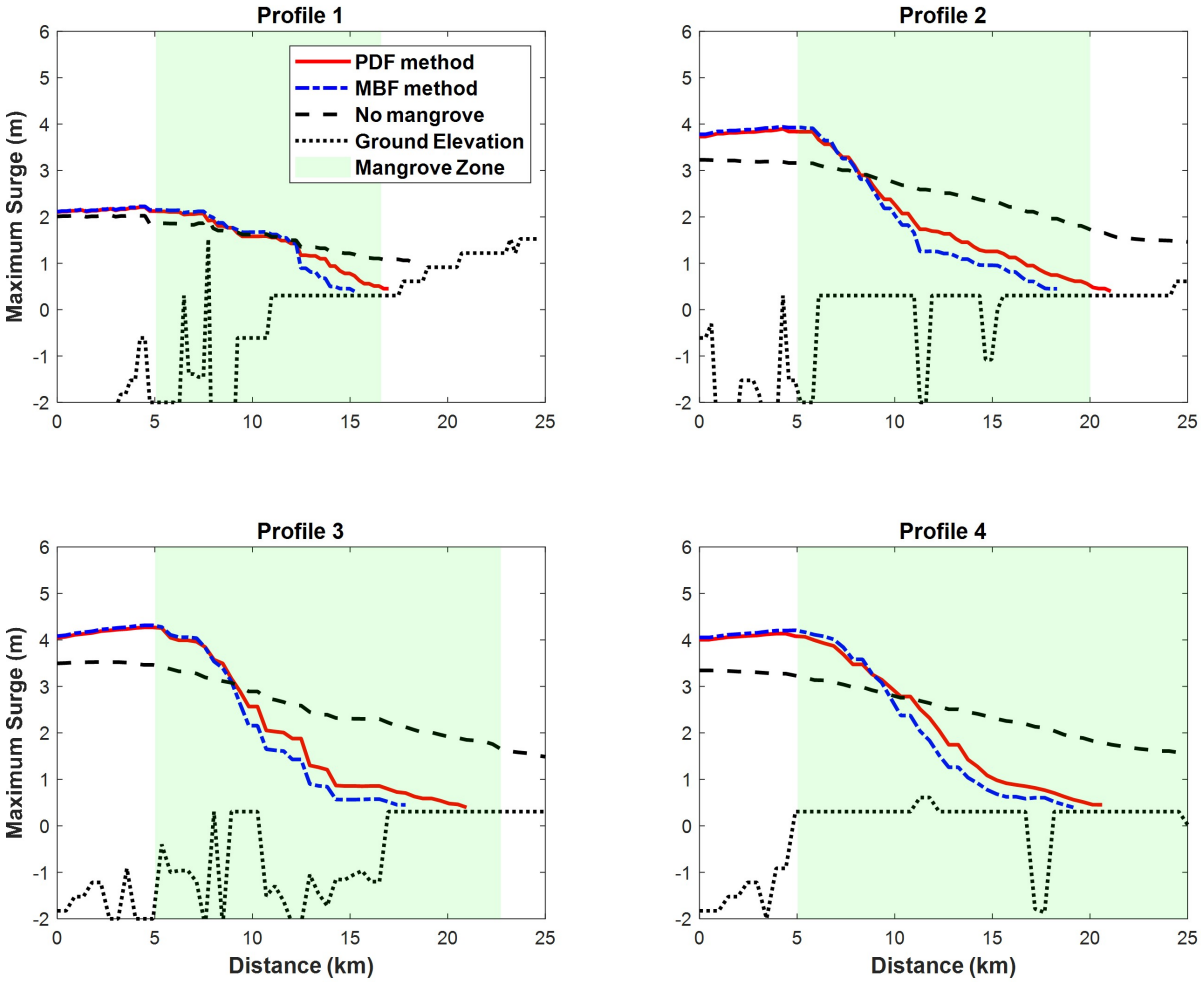

Fig. 16: Comparisons for the computed peak surge profiles along the four profiles across the mangrove zone (see Fig. 15a for the profile location).

Zhang et al. (2012) works well in the coastal areas experiencing high storm surges. The time series comparisons (Fig. 18) also show acceptable results of the simulations in both the ocean areas (NOAA tide gauges at the left panels) and the river channels (USGS stations at the right panels). It is noticeable that there are slight phase errors for the occurring time of the water elevation peaks at the river stations. This is most likely due to the fact that the current grid size is much wider than the river width in reality, and the river channels are approximated by stair-like grid cells, which leads to longer distance for water to propagate upstream in the numerical model, hence the delay of arriving time. The wider grid size also results in more water than could, in reality, moving upstream in the rivers, which may be responsible for the over-estimation of the water elevation peaks in Broad River and Chatham River (Fig. 18).

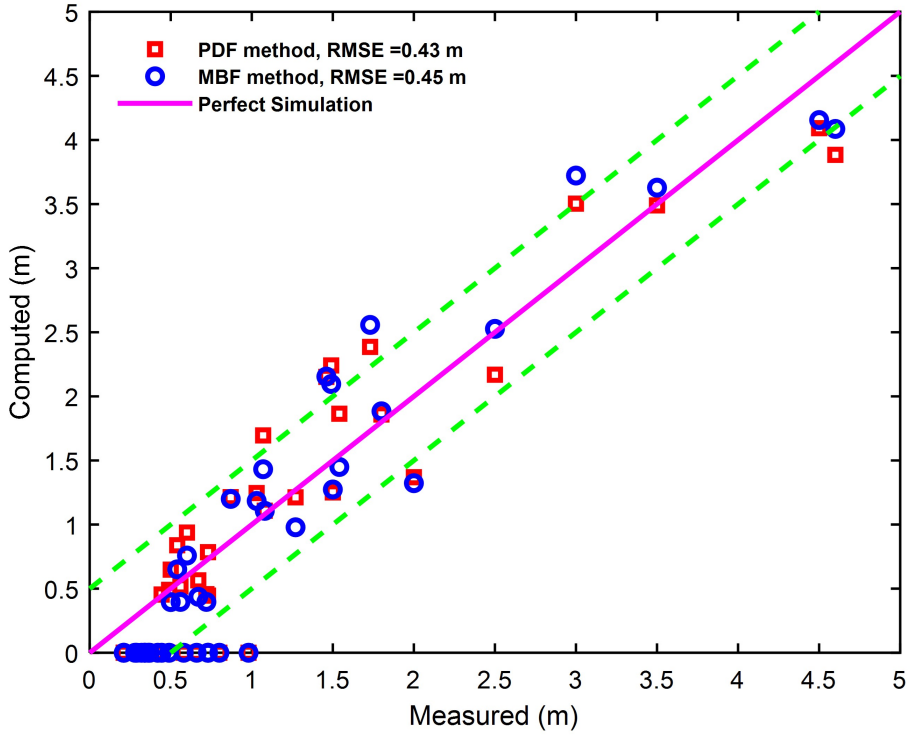

Fig. 17: Comparison between the observed peak surge heights and the computed peak surge heights (NAVD88) at the measurement locations listed in Fig. 1. The dashed lines represent the perfect simulation line ±0.5 m.

6. Discussion

This study made the assumption that the characteristics of mangrove trees within the South Florida mangrove zone are represented by those of the red mangrove, because red mangroves including forest, shrubland and scrub are the dominant species within this region according to the comprehensive vegetation map for the Everglades National Park (Ruiz et al., 2017, 2018). The vegetation characteristics of other major species in this region, including black mangrove, white mangrove and marsh, were not considered, because it is very difficult to find a consistent numerical method to represent a variety of mangrove species, and landscape scale data map of species compositions is not available. The use of an enhanced Manning coefficient map based on the land cover may provide an alternative solution to these difficulties; however, the determination of the Manning coefficient is often empirical and requires more efforts on calibration when circumstances changes. The current assumption nevertheless allows the implementation of the proposed numerical method that represents mangroves more justifiably and with more physical detail; moreover, the results

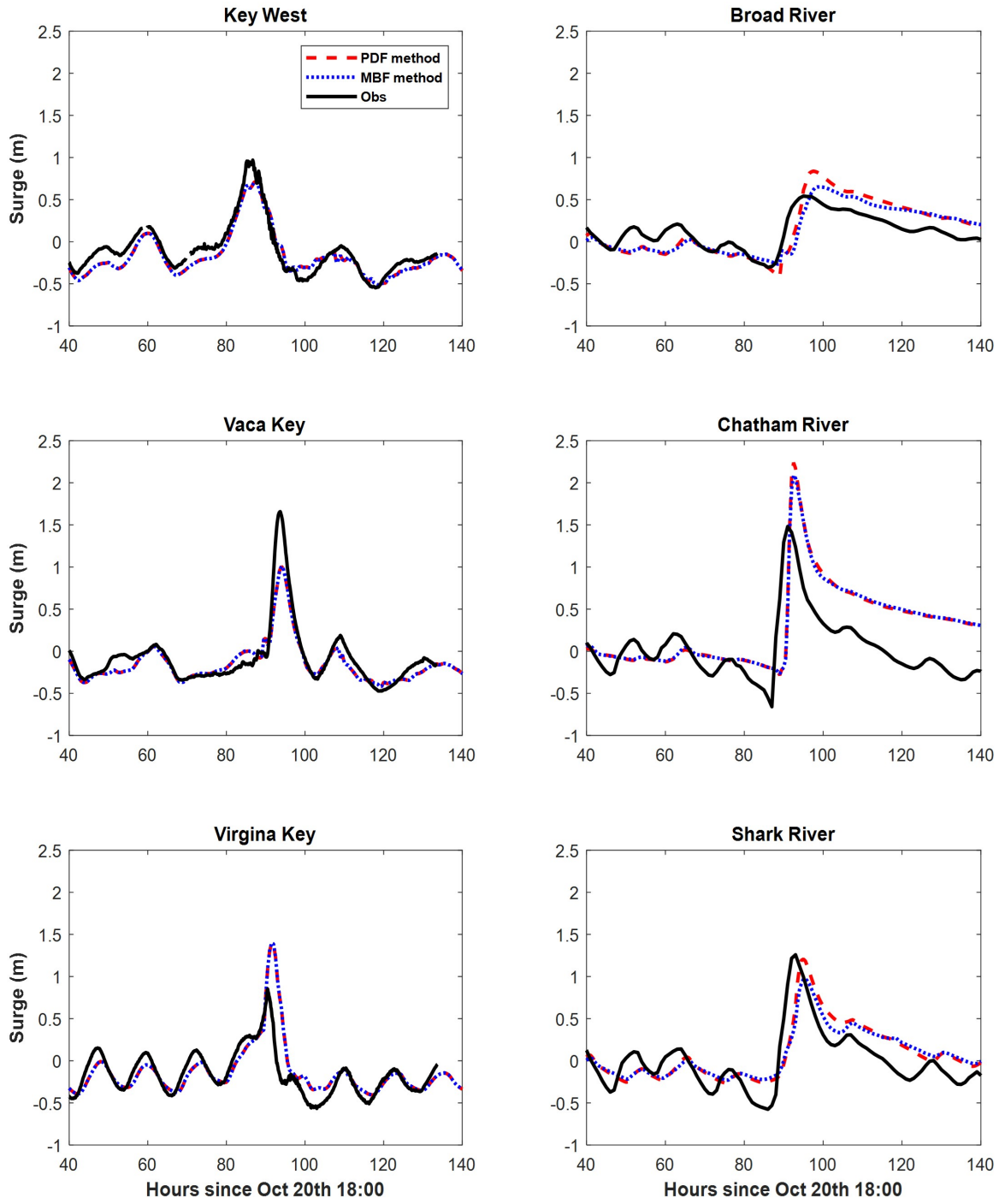

Fig. 18: Comparison for the time series of water surface elevations (NAVD88) at various stations during Hurricane Wilma (2005). The location of the stations is marked in Fig. 1.

shown in Section 5, imply that such assumption is an acceptable simplification.

The proposed PDF method in general predicted reasonably good results regarding the storm surge induced by Hurricane Wilma (2005) in the South Florida mangrove area. This is aided by the development of an advanced abstract tree model to capture major structural characteristics of mangroves as well as the use of a landscape scale data map of mean mangrove tree height. From the perspective of numerical simulation, remote sensing technology, such as radar and LiDAR, has made ecological data on mangroves available at a large scale, which encourages characterizing detailed mangrove tree structures at a small scale. Efficient combination of such small and large scale data with sophisticated numerical models could provide effective estimation of the attenuation effect of mangrove zones, and suggest the appropriate management of such zones for protecting the communities that lie behind these zones. Furthermore, to give suitable solutions for targeted areas, development based on the current tree model for red mangroves, or other mangrove species, as well as the utilization of associated allometric equations, may be necessary to better reflect local mangrove tree characteristics. This is because the characteristics of mangrove trees, even those of the same species, vary significantly both spatially and temporally (see data in Mazda et al. (1997)). In addition to this, local storm surge behavior is also affected by many other factors such as ground elevation, rainfall and hurricane characteristics (Zhang et al., 2012).

Throughout the current study, extensive comparisons between the results obtained by the PDF method and the MBF method have been made. As demonstrated in Section 4.3, the fundamental difference between the two methods lies in the coefficients associated with the velocity quadratic term in the drag force and the bed friction force terms, respectively. The coefficient in the PDF method incorporates both mangrove tree structural and ecological details, hence it exhibits more variation in its relation to the water depth than the one does for the MBF method. In the test case of Hurricane Wilma (2005), the PDF method in general predicts larger inundation extents when compared with the MBF method, while both methods give similar peak water elevations at the front of the mangrove zone. Hence, the PDF method predicts a smaller decay rate of storm surge attributable to the mangroves than the MBF method does. This is largely because that as the water propagates further inland, the water depth becomes smaller and smaller, where the MBF method coefficient becomes significantly larger than that of the PDF method. While the MBF method may predict overly large mangrove resistance to the water flows when the water depth is small, the PDF method could underestimate the resistance due to the highly simplified parameterization of turbulence within the 2D CEST model. Nevertheless, comparisons against field observations

show that the use of a Manning coefficient of 1.4, as suggested by Zhang et al. (2012), worked well for the mangrove zone in the study area. Importantly, the proposed PDF method achieved better results when simulating the storm surge inundation area and also a more accurate quantification of the attenuation of storm surge due to mangroves.

The attenuation rate of mangroves on storm surge is an important parameter for quantifying mangrove effects and was investigated at various sites globally through field observation (Krauss et al., 2009; Montgomery et al., 2018), numerical modeling (Zhang et al., 2012; Dasgupta et al., 2019) and theoretical analysis (Montgomery et al., 2019). However, there exists no consistent conclusion with regard to such attenuation rates, that ranges from some 4 to 50 cm/km (Krauss et al., 2009; Zhang et al., 2012; Montgomery et al., 2018; Vafeidis et al., 2019). One of the reasons is that it is very difficult to separate the contributions of mangroves over many other factors that could also affect the peak water level of storm surge. For example, the storm surge is affected by the geometry of the coastline (e.g. funnel-shaped estuary could increase surge level) and topography characteristics inland (e.g. channel networks can reduce mangrove influence (Montgomery et al., 2018)) even without any vegetation cover. It could be problematic to directly apply the attenuation rates from one site to another. For the mangrove zone along the coast of Southwest Florida, Krauss et al. (2009) estimated mangrove attenuation rates of 4.2 to 9.4 cm/km based on Hurricane Charley (2004) and Wilma (2005). Their estimations, however, are based on sparse gauge measurements referenced to the ground level, which increase uncertainty of the records being affected by local topography (Zhang et al., 2012). Also pointed out by Zhang et al. (2012), the calculations by Krauss et al. (2009) do not consider the high water level at the front of the mangrove zone (see the comparison of peak water levels with and without the mangroves in Fig. 16). Observations by Montgomery et al. (2018) show that much of the surge dissipation occurred at the seaward fringe of the mangrove forest, as also seen in Fig. 16. Therefore, the averaged mangrove attenuation rates could be significantly underestimated by Krauss et al. (2009). On the other hand, Zhang et al. (2012), through numerical modeling on the same mangrove area, suggested mangrove attenuation rates of up to 48 cm/km. However, their numerical simulations do not include the tidal effects, which also add uncertainty as the water level change attributed to the tidal effects would influence mangrove resistances to the flows. In addition, in the simulations of Zhang et al. (2012), the drag force due to mangroves is estimated by using the Manning coefficient based friction force, which completely ignores the ecological characteristics of mangroves at both small and large scales. In the current numerical study, both of the above-mentioned aspects have been accounted for,

and the results indicate mangrove attenuation rates of approximately 18 to 24 cm/km from mixed mangrove islands and open water to dense mangrove forests, which agrees with the attenuation rate of 24 cm/km for unchannelized mangrove forests suggested by Montgomery et al. (2018).

7. Conclusions

The CEST model, incorporating the porosity plus drag force method for modeling the mangrove effect on attenuating storm surges, generated good results for simulating the storm surge across the South Florida mangrove zone caused by Hurricane Wilma (2005). These include good agreements with field measurements or observations for the maximum surge height, inundation extend, HWMs and time series of surface elevations at tidal gauges and river stations. The numerical model predicted a maximum surge height of approximately 4.3 m between Chatham River and Shark River. The computed decay rate of the peak storm surge height was approximately 18 cm/km across the areas with a mixture of mangrove islands and open water and 24 cm/km through dense mangrove forest areas. Results show that short mangrove trees ($T < 4$ m) can be more effective than tall mangrove trees on storm surge attenuation when the water depth is relatively low ($H < 4$ m). The porosity (volume exclusion) term played a negligible role and can be ignored, because the volume ratio of mangrove to the total volume of mangrove and water on the same area is very low within the study area.

Compared to the Manning coefficient method, the porosity plus drag force method predicted better results of the inundation extents of the storm surge across the mangrove zone caused by Hurricane Wilma (2005). Particularly, the porosity plus drag force method produced approximately 1.5 km to 3 km larger inundation distance to the shoreline than the Manning coefficient method did, resulting in roughly 350 km^2 more inundation area. Both methods generated very similar maximum surge heights at the front of the mangrove zone, and consequently, the porosity plus drag force method suggested approximately 4 cm/km to 5 cm/km smaller decay rates of storm surge than that obtained by the Manning coefficient method. Based on the current study, a plot showing the fundamental difference between the drag force due to the porosity plus drag force method and the bed friction force owing to the Manning coefficient method was produced (Fig. 13). In general, the variation of the drag force depends on the flow velocity, water depth and the mangrove ecological characteristics at both large and small scales. The porosity plus drag force method would benefit from the inclusion of a species composition map, and more diverse tree models representing various

mangrove species.

Acknowledgements

We thank the reviewers for their constructive comments and suggestions on improving the quality of this paper. This work is supported by the USA National Science Foundation under Award Number 1801244, and Florida Office of Insurance Regulation under the Florida Public Hurricane Loss Model (FPHLM) project.

References

Blumberg, A. F., Herring, H. J., 1987. Circulation modelling using orthogonal curvilinear coordinates. In: Nihoul, J. C. J., Jamart, B. M. (Eds.), Three-Dimensional Models of Marine and Estuarine Dynamics. Vol. 45 of Elsevier Oceanography Series. Elsevier, pp. 55 – 88.
URL http://www.sciencedirect.com/science/article/pii/S0422989408704422

Dasgupta, S., Islam, M. S., Huq, M., Huque Khan, Z., Hasib, M. R., 03 2019. Quantifying the protective capacity of mangroves from storm surges in coastal Bangladesh. PLOS ONE 14 (3), 1–14.
URL https://doi.org/10.1371/journal.pone.0214079

Feliciano, E. A., Wdowinski, S., Potts, M. D., Lee, S.-K., Fatoyinbo, T. E., 2017. Estimating mangrove canopy height and above-ground biomass in the Everglades National Park with airborne LiDAR and TanDEM-X data. Remote Sensing 9 (7).
URL https://www.mdpi.com/2072-4292/9/7/702

Hervouet, J.-M., Samie, R., Moreau, B., 2000. Modelling urban areas in dam-break flood-wave numerical simulations. In: Proceedings of the International Seminar and Workshop on Rescue Actions Based on Dambreak Flow Analysis. Seinajoki, Finland.

Hirata, Y., Tabuchi, R., Patanaponpaiboon, P., Poungparn, S., Yoneda, R., Fujioka, Y., 2014. Estimation of aboveground biomass in mangrove forests using high-resolution satellite data. Journal of Forest Research 19 (1), 34–41.
URL https://doi.org/10.1007/s10310-013-0402-5

Horstman, E. M., Dohmen-Janssen, C. M., Narra, P. M. F., van den Berg, N. J. F., Siemerink, M., Hulscher, S. J. M. H., 2014. Wave attenuation in mangroves: A quantitative approach to field observations. Coastal Engineering 94, 47–62.
URL https://www.sciencedirect.com/science/article/pii/S0378383914001574

Iimura, K., Tanaka, N., 2012. Numerical simulation estimating effects of tree density distribution in coastal forest on tsunami mitigation. Ocean Engineering 54, 223 – 232.
URL http://www.sciencedirect.com/science/article/pii/S0029801812002806

Jelesnianski, C. P., Chen, J., Shaffer, W. A., 1992. SLOSH: Sea, Lake, and Overland Surges from Hurricanes. NOAA technical report NWS. U.S. Department of Commerce, National Oceanic and Atmospheric Administration, National Weather Service.
URL https://books.google.com/books?id=Wdg8mQfzkVcC

Krauss, K. W., Doyle, T. W., Doyle, T. J., Swarzenski, C. M., From, A. S., Day, R. H., Conner, W. H., 2009. Water level observations in mangrove swamps during two hurricanes in Florida. Wetlands 29 (1), 142–149.

Liu, H., Zhang, K., Li, Y., Xie, L., 2013. Numerical study of the sensitivity of mangroves in reducing storm surge and flooding to hurricane characteristics in southern Florida. Continental Shelf Research 64, 51 – 65.
URL http://www.sciencedirect.com/science/article/pii/S0278434313001994

Mazda, Y., Wolanski, E., King, B., Sase, A., Ohtsuka, D., Magi, M., 1997. Drag force due to vegetation in mangrove swamps. Mangroves and salt marshes 1 (3), 193–199.

Montgomery, J. M., Bryan, K. R., Horstman, E. M., Mullarney, J. C., 2018. Attenuation of tides and surges by mangroves: Contrasting case studies from New Zealand. Water 10 (9).
URL https://www.mdpi.com/2073-4441/10/9/1119

Montgomery, J. M., Bryan, K. R., Mullarney, J. C., Horstman, E. M., 2019. Attenuation of storm surges by coastal mangroves. Geophysical Research Letters 46 (5), 2680–2689.
URL https://agupubs.onlinelibrary.wiley.com/doi/abs/10.1029/2018GL081636

Mugasha, W. A., Mauya, E. W., Njana, A. M., Karlsson, K., Malimbwi, R. E., Ernest, S., 2019. Height-diameter allometry for tree species in Tanzania Mainland. International Journal of Forestry Research 2019, 1–17.

Mukai, A. Y., Westerink, J. J., Luettich, R. A., J., Mark, D., 2002. Eastcoast 2001, a tidal constituent database for Western North Atlantic, Gulf of Mexico, and Caribbean Sea. Report ERDC/CHL TR-02-24, U.S. Army Corps of Engineers, Washington, DC.

Nepf, H. M., 1999. Drag, turbulence, and diffusion in flow through emergent vegetation. Water Resources Research 35 (2), 479–489.
URL https://agupubs.onlinelibrary.wiley.com/doi/abs/10.1029/1998WR900069

Pasch, R. J., Blake, E. S., Cobb III, H. D., Roberts, D. P., January 2006. Tropical cyclone report Hurricane Wilma 15-25 October 2005. Tech. rep., National Hurricane Center, NOAA, USA, Miami, Florida.
URL https://www.nhc.noaa.gov/data/tcr/AL252005_Wilma.pdf

Powell, M. D., Houston, S. H., Amat, L. R., Morisseau-Leroy, N., 1998. The HRD real-time hurricane wind analysis system. Journal of Wind Engineering and Industrial Aerodynamics 77-78, 53 – 64.
URL http://www.sciencedirect.com/science/article/pii/S0167610598001317

Rodríguez, J. F., Saco, P. M., Sandi, S., Saintilan, N., Riccardi, G., 2017. Potential increase in coastal wetland vulnerability to sea-level rise suggested by considering hydrodynamic attenuation effects. Nature communications 8 (1), 1–12.

Ross, M. S., Ruiz, P. L., Telesnicki, G. J., Meeder, J. F., 2001. Estimating above-ground biomass and production in mangrove communities of Biscayne National Park, Florida (USA). Wetlands Ecology and Management 9 (1), 27–37.

Ruiz, P., Giannini, H., Prats, M., Perry, C., Foguer, M., Garcia, A., Shamblin, B., Whelan, K., Hernandez, M.-J., 2017. The everglades national park and big cypress national preserve vegetation mapping project interim report-southeast saline everglades (region 2), everglades national park. Report Natural Resource Report NPS/SFCN/NRR—2017/1494, National Park Service, Fort Collins, Colorado.

Ruiz, P., Prats, M., Perry, C., Garcia, A., Foguer, M., Ingram, J., Shamblin, R., Guichardot, M., Whelan, K.,

2018. The everglades national park and big cypress national preserve vegetation mapping project interim report-southwest coastal everglades (region 3), everglades national park. Report Natural Resource Report NPS/SFCN/NRR–1776, National Park Service, Fort Collins, Colorado.

Sheng, Y. P., Zou, R., 2017. Assessing the role of mangrove forest in reducing coastal inundation during major hurricanes. Hydrobiologia 803 (1), 87–103.

Simard, M., Zhang, K., Rivera-Monroy, V. H., Ross, M. S., Ruiz, P. L., Castañeda-Moya, E., Twilley, R. R., Rodriguez, E., 2006. Mapping height and biomass of mangrove forests in Everglades National Park with SRTM elevation data. Photogrammetric Engineering & Remote Sensing 72 (3), 299–311.

Smith, T. J., Anderson, G. H., Balentine, K., Tiling, G., Ward, G. A., Whelan, K. R. T., 2009. Cumulative impacts of hurricanes on Florida mangrove ecosystems: sediment deposition, storm surges and vegetation. Wetlands 29 (1), 24–34.

Smith, T. J., Whelan, K. R. T., 2006. Development of allometric relations for three mangrove species in South Florida for use in the Greater Everglades Ecosystem restoration. Wetlands Ecology and Management 14 (5), 409–419.

Soderqvist, L. E., Byrne, M. J., 2007. Monitoring the storm tide of Hurricane Wilma in southwestern Florida, October 2005. US Geological Survey Reston, VA, USA.
URL http://pubs.er.usgs.gov/publication/ds294

Stone, B. M., Shen, H. T., 2002. Hydraulic resistance of flow in channels with cylindrical roughness. Journal of Hydraulic Engineering 128 (5), 500–506.

Tamai, S., Nakasuga, T., Tabuchi, R., Ogino, K., 1986. Standing biomass of mangrove forests in southern Thailand. Journal of the japanese forestry society 68 (9), 384–388.

Tanaka, N., 2009. Vegetation bioshields for tsunami mitigation: review of effectiveness, limitations, construction, and sustainable management. Landscape and Ecological Engineering 5 (1), 71–79.

Tanaka, N., Sasaki, Y., Mowjood, M. I. M., Jinadasa, K. B. S. N.and Homchuen, S., 2007. Coastal vegetation structures and their functions in tsunami protection: experience of the recent Indian Ocean tsunami. Landscape and Ecological Engineering 3 (1), 33–45.

Teh, S. Y., Koh, H. L., Liu, P. L., Ismail, A. I. M., Lee, H. L., 2009. Analytical and numerical simulation of tsunami mitigation by mangroves in Penang, Malaysia. Journal of Asian Earth Sciences 36 (1), 38 – 46, tsunamis in Asia.
URL http://www.sciencedirect.com/science/article/pii/S1367912008001557

Telis, P. A., 2006. The Everglades Depth Estimation Network (EDEN) for support of ecological and biological assessments. Report 2006-3087, Geological Survey (U.S.).

Temmerman, S., Meire, P., Bouma, T. J., Herman, P. M. J., Ysebaert, T., De Vriend, H. J., 2013. Ecosystem-based coastal defence in the face of global change. Nature 504 (7478), 79–83.

Tomiczek, T., Wargula, A., Lomónaco, P., Goodwin, S., Cox, D., Kennedy, A., Lynett, P., 2020. Physical model investigation of mid-scale mangrove effects on flow hydrodynamics and pressures and loads in the built environment. Coastal Engineering 162, 103791.
URL https://www.sciencedirect.com/science/article/pii/S0378383920304774

Vafeidis, A. T., Schuerch, M., Wolff, C., Spencer, T., Merkens, J. L., Hinkel, J., Lincke, D., Brown, S., Nicholls, R. J., 2019. Water-level attenuation in global-scale assessments of exposure to coastal flooding: a sensitivity analysis. Natural Hazards and Earth System Sciences 19 (5), 973–984.

URL https://nhess.copernicus.org/articles/19/973/2019/

Ward, G. A., Smith, T. J., Whelan, K. R. T., Doyle, T. W., 2006. Regional processes in mangrove ecosystems: spatial scaling relationships, biomass, and turnover rates following catastrophic disturbance. Hydrobiologia 569 (1), 517–527.

Wu, W., Marsooli, R., 2012. A depth-averaged 2D shallow water model for breaking and non-breaking long waves affected by rigid vegetation. Journal of Hydraulic Research 50 (6), 558–575.
URL https://doi.org/10.1080/00221686.2012.734534

Wu, Y., Falconer, R., Struve, J., 2001. Mathematical modelling of tidal currents in mangrove forests. Environmental Modelling & Software 16 (1), 19 – 29.
URL http://www.sciencedirect.com/science/article/pii/S1364815200000591

Xu, H., Zhang, K., Shen, J., Li, Y., 2010. Storm surge simulation along the US East and Gulf Coasts using a multi-scale numerical model approach. Ocean Dynamics 60 (6), 1597–1619.

Zhang, K., Li, Y., Liu, H., Rhome, J., Forbes, C., 2013. Transition of the coastal and estuarine storm tide model to an operational storm surge forecast model: A case study of the Florida coast. Weather and Forecasting 28 (4), 1019 – 1037.
URL https://journals.ametsoc.org/view/journals/wefo/28/4/waf-d-12-00076_1.xml

Zhang, K., Liu, H., Li, Y., Xu, H., Shen, J., Rhome, J., Smith, T. J., 2012. The role of mangroves in attenuating storm surges. Estuarine, Coastal and Shelf Science 102-103, 11 – 23.
URL http://www.sciencedirect.com/science/article/pii/S0272771412000674

Zhang, K., Thapa, B., Ross, M., Gann, D., 2016. Remote sensing of seasonal changes and disturbances in mangrove forest: a case study from South Florida. Ecosphere 7 (6), e01366.
URL https://esajournals.onlinelibrary.wiley.com/doi/abs/10.1002/ecs2.1366

Zhang, K., Xiao, C., Shen, J., 2008. Comparison of the CEST and SLOSH models for storm surge flooding. Journal of Coastal Research 24 (2 (242)), 489–499.

Zhang, Y., Yang, Y., Yang, K., Tan, X., Sun, X., Leng, B., Zhou, C., Zhu, B., 2020. Non-linear wave attenuation quantification model improves the estimation of wave attenuation efficiency of mangroves. Estuarine, Coastal and Shelf Science 245, 106927.
URL https://www.sciencedirect.com/science/article/pii/S0272771420306582